Pure and Applied Geophysics

The 2007 Medea Seismic Sequence, North-Central Algeria: Source Parameters, Stress Tensor, and Static Stress Changes

G. Dabouz,[1,2] H. Beldjoudi,[1] B. Delouis,[3] O. Boulahia,[1] Y. Mohammedi,[1] and A. Yelles-Chaouche[1]

Abstract—Dense seismic networks provide the opportunity to better understand seismogenic processes in tectonically active regions. The Algerian Digital Seismic Network was strengthened following the 10 October 1980 Ms 7.3 El Asnam and 21 May 2003 Mw 6.8 Bournerdes earthquakes, such that the source parameters of small- to moderate-magnitude earthquakes in northern Algeria can now be computed. Here we examine the 2007 seismic sequence recorded in the Medea region (north-central part of Algeria). We calculate the seismic sources of three moderate events that occurred between May and August 2007 using near-field waveform modeling, and obtain moment magnitudes of 4.4, 4.1, and 4.6, with fault planes oriented N63°E, N15°E, and N219°E, respectively. We use displacement spectra to estimate the corner frequency f_c and spectral flat level then use these to recalculate the seismic moment and moment magnitude. The stress tensor obtained by inverting 13 focal mechanisms from events near the 2007 sequence exhibits a well-constrained compressional axis with a subhorizontal N335°E-trending σ_1 axis (plunge 7°). We calculate the static stress changes to understand the connections between these three events. The results indicate an interaction between the faults related to these events during the earthquake sequence. We conclude that these events likely occurred on the unstudied extensions of mapped faults, and that the epicentral area therefore has moderate seismogenic potential.

Keywords: Waveform modeling, source parameters, Medea seismicity, Algeria, Tellian Atlas, Coulomb stress transfer.

1. Introduction

Algeria is among the most seismically active countries of north Africa due to convergence of the African and Eurasian plates at rates of 4–5 mm/year (Bougrine et al., 2019; Calais et al., 2003; Nocquet & Calais, 2004; Palano et al., 2015; Serpelloni et al., 2007). Stress is accommodated by active faults and folds in the offshore, Tell Atlas, high plateaus, and Saharan Atlas regions (Domzig, 2006; Meghraoui & Pondrelli, 2012). Seismicity principally occurs on reverse faults and faulted folds associated with Neogene border basins, such as the Cheliff, Mitidja, and Medea basins (Meghraoui, 1988). Active faults are mainly oriented NE–SW, and are related to a compressive stress regime.

Many historical events have been reported in northern Algeria since 1365 AD; starting with the most destructive events in 1365 and 1716 in the region of Algiers and in 1790 in the region of Oran, all with an intensity of ($I_0 = X$). On 10 October 1980, an earthquake with *Ms* 7.3 struck the El Asnam region which was the strongest event recorded in the western part of the Mediterranean area; another event hit the city of Boumerdes on 21 May 2003 with *Mw* 6.8, located ∼ 80 km NE of the Medea region (Fig. 1).

The Medea region is located in the Tell Atlas, 60 km southwest of Algiers, the capital of Algeria. The geography is roughly characterized as a high-elevation rough terrain that encloses some flatter extensional plains (Fig. 2). A moderate *Mw* 4.4 earthquake initiated a seismic sequence in the region on 8 May 2007. Two moderate events followed on 21 and 22 August 2007 (*Mw* 4.1 and *Mw* 4.6, respectively; Table 1). A swarm of aftershocks were recorded between 21 August and 25 September 2007. There was no reported damage associated with this seismic sequence. Historical and instrumental catalogs indicate that the epicentral area has not

[1] Centre de Recherche en Astronomie, Astrophysique et Géophysique, B.P. 63-Bouzaréah, 16340 Alger, Algérie. E-mail: ghania.dabouz@craag.edu.dz
[2] Université Abou Bekr Belkaid 22, Rue Abi Ayed Abdelkrim Fg Pasteur B.P 119, 13000 Tlemcen, Algérie.
[3] Géoazur, Université de Nice Sophia Antipolis, Observatoire de la Côte d'Azur, CNRS, 250 rue Albert Einstein, 06560 Valbonne, France.
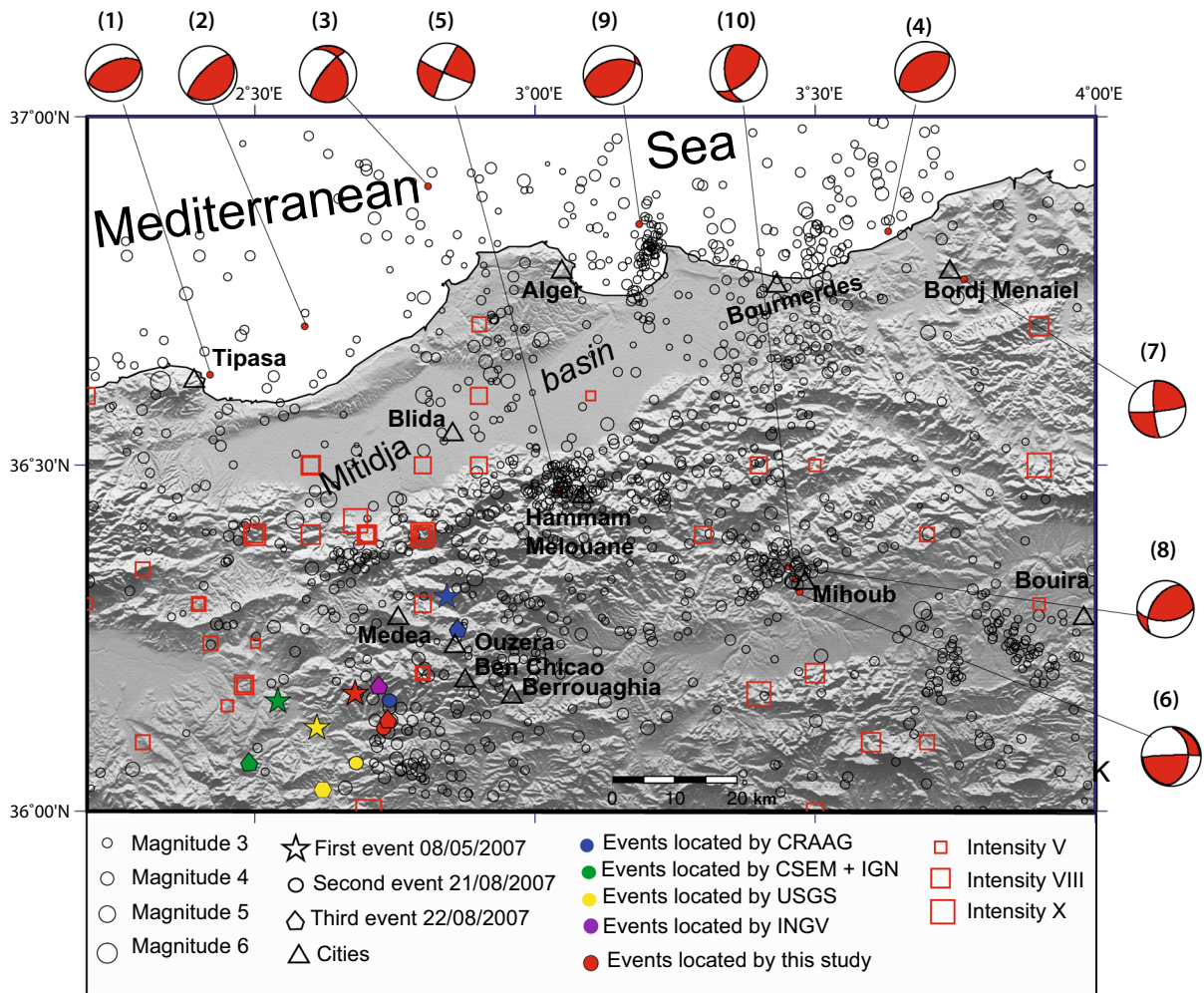
Figure 1

Historical and instrumental seismicity in the Medea region from 1825 to 2017. Red open squares show historical earthquakes. Black open circles show instrumental seismicity. Star, circle, and polygon show the first, second, and third events, respectively. Colors; red, green, yellow, purple, and blue represent locations given by different seismologic centers. Black open triangles represent cities and villages. The focal mechanisms of significant earthquakes in the region are numbered: (1) 29 September 1989 *Mw* 6.0 Mont-Chenoua (Tipasa) earthquake (Bounif et al., 2003); (2) 2 September 1990 *Mw* 4.7 Tipaza earthquake (Sebaï & Ouahmed, 1997); (3) 4 September 1996 *Mw* 5.6 Ain Benian earthquake (Sebaï & Ouahmed, 1997); (4) 21 May 2003 *Mw* 6.0 Boumerdes-Zemmouri earthquake (Ayadi et al., 2003; Bounif et al., 2004); (5) 17 July 2013 *Mw* 5.0 Hammam-Melouane earthquake (Yelles-Chaouche et al., 2017); (6) 23 May 2013 *Ml* 4.2 Mihoub earthquake (Khelif et al., 2018); (7) 22 February 2014 *Mw* 4.1 Bordj Menaiel earthquake (Semmane et al., 2015); (8) 15 November 2014 *Mw* 4.3 Mihoub earthquake (Semmane et al., 2017); (9) 1 August 2014 *Mw* 5.7 Algiers Bay earthquake (Beldjoudi, 2017); (10) 28 May 2016 *Mw* 5.4 Mihoub earthquake (Khelif et al., 2018)

experienced any other significant events. While many geological studies have been conducted in this area, (Boudiaf, 1996; Caire, 1957; Guiraud, 1977; Kieken, 1974; Roman, 1975) seismological studies of this tectonically active environment are scarce.

Here we calculate the seismic source parameters for the three moderate main events in the 2007 Medea

seismic sequence using two methods: near-field waveform modeling (FMNEAR) (Delouis, 2014) and source spectrum modeling (Abacha et al., 2018). The source parameters computed by these two methods are the moment magnitude (*Mw*), focal mechanism (strike, dip, and rake), and seismic moment (*M*$_0$). We analyze the seismic sources of the main events in the
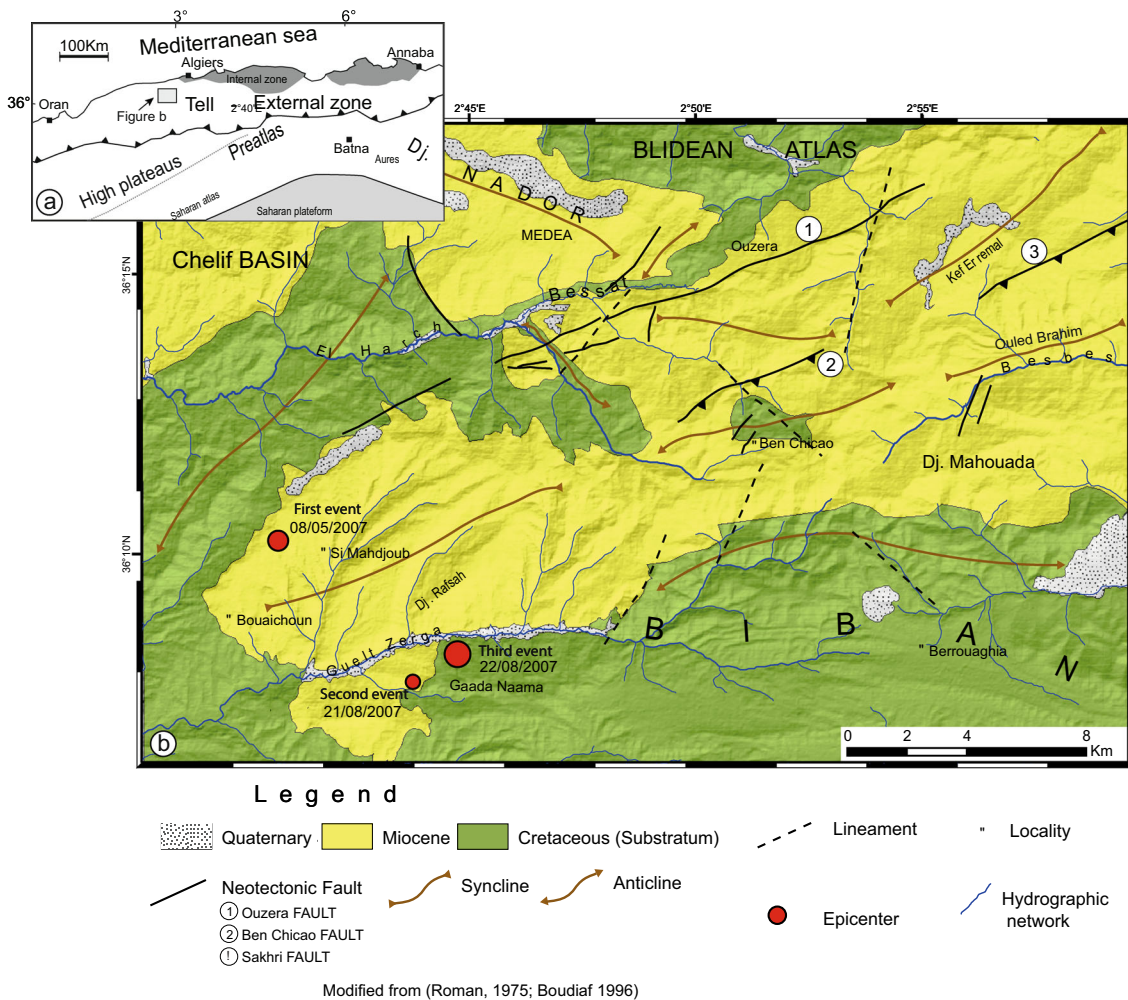
Figure 2
a General tectonic domains of the Algerian Tell Atlas (Durand-Delga et al., 1970; Meghraoui, 1988; Wildi, 1983). **b** Geological map of the epicentral area [modified from Roman (1975) and Boudiaf (1996)]. Red circles show epicenters of main events

sequence using broadband seismogram records from the Algerian Digital Seismic Network (ADSN) to determine whether these events are connected. Then, we calculate the stress tensor in the region, compute the regional Coulomb stress failure criterion and finally discuss the implications for the regional stress state. This study advances our understanding of seismicity in the Medea region and the geological structures responsible for the 2007 Medea seismic sequence.

2. Historical and Instrumental Seismicity

Rothé et al. (1950) found two large earthquakes in historical accounts of the Medea region and surrounding area. The first occurred on 2 March 1825, and had a maximum intensity $I_0 = X$ in the city of Blida and two neighboring villages; it was reported that many people were trapped under rubble, with few survivors. This event was felt as far away as Algiers. The second occurred on 2 January 1867, with a maximum intensity $I_0 = X$, and was observed in the southern locality of Blida. Light damage was reported in the Medea-area villages that were located ~ 30

Origin time UTC (hh:mm:ss)	Lat. ° N	Long. ° E	Depth (km)	Magnitude	Ref.
First event 08/05/2007					
06:56:34	36.17	2.68	5	Mw = 4.4	This study
06:56:34	36.31	2.84	2.7	Md = 4.8	CRAAG
06:56:34	36.16	2.54	10	Mb = 4.5	CSEM
06:56:35	36.12	2.61	3.5	Mw = 4.0	USGS
06:56:30	35.90	2.62	12	Mw = 4.3	INGV
06:56:35	36.16	2.54	10	Mw = 4.2	IGN
Second event 21/08/2007					
14:58:42	36.12	2.73	13.5	Mw = 4.1	This study
14:58:42	36.16	2.74	1.3	Md = 4.7	CRAAG
14:58:41	36.07	2.68	10	Mw = 4.4	USGS
Third event 22/08/2007					
18:08:35	36.13	2.74	14	Mw = 4.6	This study
18:08:35	36.26	2.86	5	Md = 5.2	CRAAG
18:08:35	36.07	2.49	30	Mb = 4.4	CSEM
18:08:34	36.03	2.62	12	Mw = 4.6	USGS
18:08:35	36.18	2.72	12	Mw = 4.4	INGV
18:08:36	36.07	2.49	30	Mw = 4.4	IGN

Lat. latitude; *Long.* longitude; *Ref.* reference for the event location; *CRAAG* Centre de Recherche en Astronomie, Astrophysique et Géophysique, Algeria; *EMSC-CSEM* Euro-Med Seismological Center; *USGS* United States Geological Survey, USA; *INGV* Instituto Nazionale Di Geofisica e Vulcanologia, Italy; *IGN* Istituto Geografico Nacional, Spain

km south of Blida (Table 2). The maximum felt intensity was $I_0 =$ VIII in the epicentral region of the 2007 Medea sequence (Fig. 1 and Table 2); see also (Mokrane et al., 1994). Boudiaf (1996) reported a few events in the Medea region, with maximum intensities $I_0 =$ IV in the village of Ben Chicao and $I_0 =$ VII in Medea city (Table 2). These events are located in the western part of the Medea region (Fig. 1).

The Medea region is characterized by low to moderate instrumental seismic activity compared to other active regions, such as the northern coast of Algeria (Fig. 1); however, the maximum magnitude recorded in southeastern Medea was M 4.3 from the onset of the instrumental era 1971 to 2007. No significant events were recorded or reported in the

western part of the region (Fig. 1). Additional ADSN stations were installed in late 2006 (Yelles-Chaouche et al., 2007) in response to an increase in the number of detected earthquakes. The maximum magnitude that has been recorded since the 2007 Medea seismic sequence is a Mw 5.4 event in Mihoub village, northeast of the study area (Fig. 1), on 28 May 2016 (Khelif et al., 2018). Two other moderate events were recorded on 23 May 2013 (Mw 4.2) and 15 November 2014 (Mw 4.3) in the Mihoub region (Semmane et al., 2017). These seismic sequences can be studied to improve our understanding of regional earthquake characteristics and the active geologic structures in the region.

Many moderate earthquakes have been recorded since the densification and digitization of the ADSN. Instrumental and historical records of seismicity suggest that the region is active but the seismicity rate is relatively low.

3. Geologic Setting of the Medea Region

The 2007 Medea seismic sequence was located in the post-thrust sheet of the Medea Basin situated at the southwestern border of the Blida Atlas, central Tellian Range, Algeria. The southern extent of this basin is limited by the Cretaceous Berrouaghia Chain, which represents the occidental extremity of the Biban Range (Fig. 2). The Medea Basin is formed by middle to upper Miocene formations that are considered the eastern extremities of the Cheliff Basin, which is known for its high seismic activity, notably the 1980 El Asnam Earthquake generated by the Oued Fodda fault (Meghraoui & Pondrelli, 2012).

The Medea Basin is in continuity with the Beni Sliman-Arib-Soumam Plain to the east, which experiences moderate seismic activity, e.g., the 1910 Aumale earthquake $I_0 =$ X. The tectonic structures in this region are the result of nearly N–S compressional movements of the African and Eurasian plates since the Cenozoic. Neogene post-nappe basins, which correspond to E–W-elongated intermountain structures, are characterized by compressional deformation that underwent extension during the Quaternary (Maouche et al., 2019). These neotectonic features are expressed by the development of a set of

Table 2

Significant historical earthquakes reported in the Medea region from 1633 to 1990

Date (year-month-day)	Time (hh:mm:ss)	Lat.° N	Long.° E	Intensity	Location	Ref.
1633-00-00	00:00:00	36.55	2.48		Medea	Boudiaf
1825-03-02	07:00:00	36.40	2.80	X		Rothé
1847-06-18	05:40:00	36.70	2.90	VI		Rothé
1854-05-15	15:00:00	36.40	2.70	VII		SSIS
1859-06-24	12:30:00	36.18	2.48		Medea	Boudiaf
1860-10-03	09:00:00	36.15	2.46		Medea	Boudiaf
1867-01-02	07:13:00	36.42	2.68	X		Rothé
1869-09-20	12:45:00	36.50	2.60			Rothé
1874-03-28	11:10:00	36.60	2.20	VII		Rothé
1876-03-23	06:34:00	36.50	2.60	VII		Rothé
1888-01-06	23:40:00	36.50	2.60	VIII		Rothé
1908-03-11	00:06:00	36.40	2.80	VIII		Rothé
1910-06-24	13:26:56	36.17	3.40	X	Aumale	Rothé
1914-02-03	07:15:00	36.18	2.48	V	Medea	Boudiaf
1923-02-19	17:04:00	36.10	3.70	VI		Rothé
1925-06-10	16:45:00	36.90	2.60	VIII		Rothé
1925-07-02	16:39:17	–	–	VI	Aumale	Rothé
1928-04-06	00:13:37	36.15	2.45	III	Medea	Boudiaf
1931-08-15	13:52:00	36.10	3.60	VIII		Rothé
1932-02-15	09:48:00	35.90	2.90	VII		Rothé
1936-07-06	06:14:00	36.30	2.20	V		Rothé
1938-03-02	07:43:00	36.40	2.70	VII		Rothé
1951-02-09	04:54:45	36.40	2.80	V		BH-RS
1953-07-05	01:04:15	36.20	3.50	VIII		ISS
1955-04-19	12:36:42	36.18	2.48	IV	Medea	Boudiaf
1955-07-05	10:11:54	36.10	2.30	VI		IMPGA
1955-12-03	00:57:31	36.24	2.50	IV	Ben Chicao	Boudiaf
1956-06-09	09:42:05	36.24	2.50	IV	Ben Chicao	Boudiaf
1957-01-09	15:51:36	36.24	2.42	VI		Boudiaf
1957-01-26	22:49:30	36.24	2.50	IV	Ben Chicao	Boudiaf
1957-10-19	06:08:00	36.40	3.30	VII		IMPGA
1958-03-03	13:44:30	36.18	2.48	VII	Medea	Boudiaf
1959-02-28	03:47:00	36.60	3.10	IV		IMPGA
1959-09-22	20:00:49	36.50	3.50	V		IMPGA
1960-02-20	20:33:12	36.40	2.50	VI		IMPGA
1960-08-14	21:35:18	36.60	2.90	VII		IMPGA
1961-11-23	04:45:35	36.50	2.80	VII		BCIS
1965-10-25	21:03:20	36.40	2.80	VI		IMPGA
1966-03-03	21:07:42	36.20	2.80	VI	Medea	Boudiaf
1966-04-03	05:11:39	36.50	2.80	VII		IMPGA
1966-11-11	00:38:20	36.40	2.80	V		IMPGA
1967-04-23	09:30:22	36.30	2.40	VII		IMPGA
1970-10-09	07:33:39	36.35	2.30	VI		IMPGA

Lat. latitude; *Long.* longitude; *Ref.* reference of the report (Boudiaf, 1996; Rothé et al., 1950); *SSIS* Seccion de Sismologia e Ingenieria Sismica, Spain; *ISS* International Seismological Summary, Kew Observatory, Richmond; *IMPGA* Institut de Métérologie et de Physique du Globe d'Alger, Algeria
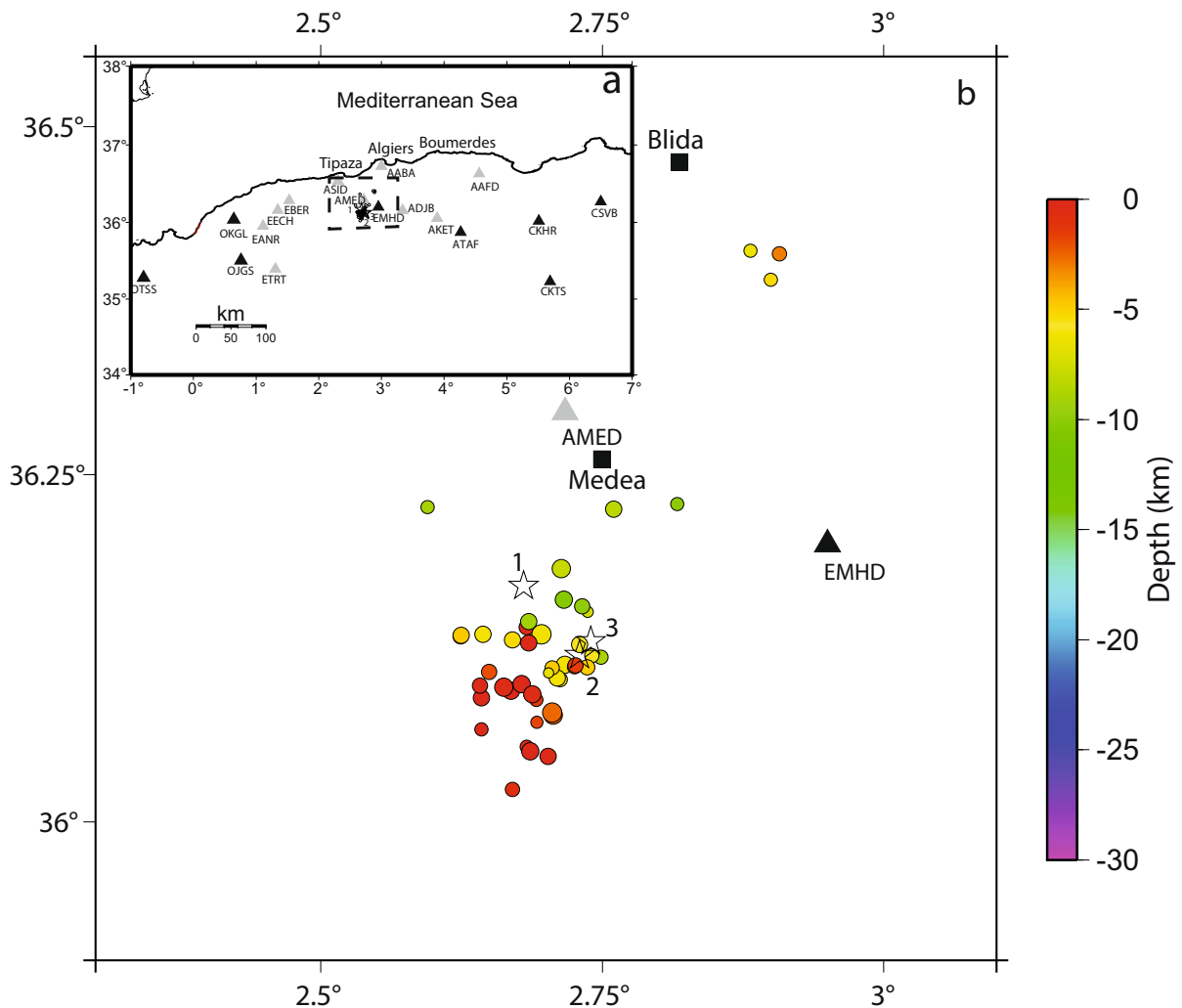
Figure 3

a Map showing the seismological network. Black triangles are broadband digital stations. Gray triangles are short-period seismic stations. Circles are locations of 58 aftershocks. The stars are the mainshock locations. **b** Zoomed-in epicentral area showing aftershock locations. Stars are the mainshock locations, respectively, number 1, 2, and 3. Colored circles are aftershocks with depth and magnitude

NE–SW-striking folds and faults. The Medea structures were initially mapped and described by Roman (1975) without relating them to the seismicity of the region. Boudiaf (1996) later examined the distribution of historic earthquakes and analyzed the morphotectonics of the region. He suggested that the tectonics especially affect the basin borders and classified these as a set of capable seismogenic faults (Fig. 2), including the following: (1) The Ouzera Fault Zone, represented by a series of parallel sub-vertical fault segments, is located in southern Medea

city, striking ∼N65°E. The northeastern extensions of the left-lateral strike-slip structures correspond to the terminating slopes along the southern border of the Blida Atlas (Boudiaf, 1996). The Ouzera Fault Zone is characterized by an inherited yet well-expressed N65°E-trending topographic scarp. (2) The Ben Chicao fault-related fold is a N65°E-striking, asymmetrical anticline with a steep dip (50–90°) along its northern flank and shallow dip (<35°) along its southern flank. The northern flank is bounded by a reverse fault with the same alignment as the axis of

Table 3

Velocity model tested to locate of the main events and aftershocks

P-wave velocity (km/s)	Depth (km)
The Algiers Bay velocity model	
5.0	00.0
5.5	01.5
6.0	07.5
7.0	15.0
8.0	22.0
The Mihoub velocity model	
3.2	00.0
4.2	00.9
5.3	01.5
6.1	14.0
6.9	21.0
The Kherrata velocity model	
4.9	00.0
6.2	11.0
6.5	15.0
Inversion velocity model	
3.3	0.0
4.5	0.6
5.5	2.0
6.5	5.0
8.1	30.0
Algiers velocity model (model selected)	
5.0	00.0
5.5	08.0
6.0	12.0
7.0	18.0
8.0	30.0

Table 4

Located epicenters of main shocks with different velocity models (Table 3) and their respective errors

Event	Model	ERH	ERZ	RMS	Long.	Lat.
First event	Algiers Bay model	1.09	2.93	0.30	2.63	36.21
	Mihoub model	1.62	1.22	0.45	2.69	36.14
	Kherrata model	1.56	1.28	0.58	2.70	36.14
	Inversion model	1.72	2.60	0.37	2.67	36.11
	Algiers model	**0.58**	**0.40**	**0.16**	2.68	**36.17**
Second event	Algiers Bay model	0.98	7.77	0.04	2.71	36.10
	Mihoub model	0.87	3.84	0.19	2.70	36.09
	Kherrata model	0.32	9.67	0.00	2.73	36.12
	Inversion model	13.0	33.9	0.21	2.73	36.11
	Algiers model	**0.35**	**0.32**	**0.01**	2.73	**36.12**
Third event	Algiers Bay model	0.90	4.90	0.02	2.72	36.10
	Mihoub model	0.93	4.08	0.20	2.70	36.09
	Kherrata model	0.20	99.0	0.02	2.74	36.13
	Inversion model	6.68	54.6	0.19	2.74	36.11
	Algiers model	**0.40**	**0.30**	**0.01**	2.74	**36.13**

Bold values denote the best result of the location of the three events obtained using the Algiers model. The same location is used thereafter

the fold, and the fault throw is estimated to be 50–100 m over a length of ~ 5 km (Boudiaf, 1996; Roman, 1975; Yelles-Chaouche et al., 2006). (3) The Sakhri Fault forms the northern limit of the Ouled Brahim Syncline and corresponds to a reverse fault plunging $\sim 70°$ toward the south. The Djebel Mahouada is a set of NE-oriented, left-lateral, strike-slip faults in this region.

4. Main Event and Aftershock Locations

The seismic sequence started on May 2007 with a first shock of Mw 4.4. No aftershocks were recorded after this first shock until 21 August 2007 at 14:58 when the second event of Mw 4.1 hit the epicentral area south of the first event, and then many aftershocks were recorded, among them the third event

with Mw 4.6 (Table 1). We have used the stations of the permanent seismic network (ADSN) for the first event and add the AMED station for the location of the remaining events (Fig. 3a). The ADSN is composed of eight broadband seismic stations (BBVS-60; Chinese product), two very broadband seismic stations (GCZ-NT 120 s; Chinese product), and 32 short-period digitized seismic stations equipped with seismometers SS1 and L22 (Beldjoudi et al., 2011; Yelles-Chaouche et al., 2013). We analyzed the records of eight broadband and ten short-period stations to locate all the events. We have used the records of five broadband seismic stations to estimate the seismic source parameters (waveform modeling and spectral amplitude). Figure 3a shows the locations of all seismic stations used in this study.

We located mainshocks and aftershocks of the Medea sequence using HYPOINVERSE software (Klein, 1978). For the three main events, we used 15 ADSN stations, including eight broadband and ten short-period stations. The geometry of our network does not present good coverage for an optimal location. We have a lack of seismologic stations in the southern part to constrain the seismic sequence. To

correct this problem, we tested several velocity models available around our epicentral area. Five velocity models were tested to improve the location (Table 3). We tested the model used in Yelles-Chaouche et al. (2017) of Algiers Bay located north of our epicentral area ∼ 50 km; the Mihoub model used in Khelif et al. (2018); this region is located east of the epicentral area (∼ 30 km); the Kherrata model used in Beldjoudi et al. (2009); this region is the farthest one from the epicentral region (∼ 120 km) to the east; the model used in this study for the waveform modeling (Delouis, 2014; Delouis et al.,

Table 5

Characteristics of the broadband stations used in the waveform modeling of the main events

Stations	Δ (km)	Filter (Hz)
First shock		
NEMHD	24	BP 0.03 0.06
ZEMHD	24	BP 0.06 0.11
NCSVB	343	BP 0.03 0.06
ZCSVB	343	BP 0.03 0.06
NOJGS	153	BP 0.03 0.06
EOJGS	153	BP 0.03 0.06
ZOJGS	153	BP 0.03 0.06
NOKGL	182	BP 0.03 0.06
ZOKGL	182	BP 0.03 0.06
Second shock		
NEMHD	20	BP 0.03 0.06
ZEMHD	20	BP 0.03 0.06
NATAF	138	BP 0.03 0.06
EATAF	138	BP 0.05 0.10
ZATAF	138	BP 0.03 0.06
NOJGS	157	BP 0.11 0.17
ZOJGS	157	BP 0.03 0.06
ZOKGL	186	BP 0.03 0.06
Third shock		
NEMHD	18	BP 0.03 0.06
ZEMHD	18	BP 0.03 0.06
NATAF	136	BP 0.03 0.06
EATAF	136	BP 0.05 0.10
ZATAF	136	BP 0.03 0.06
NOJGS	159	BP 0.11 0.17
ZOJGS	159	BP 0.03 0.06
EOKGL	188	BP 0.04 0.09
ZOKGL	188	BP 0.03 0.06
NCKTR	266	BP 0.03 0.06
ECKTR	266	BP 0.03 0.06
ZCKTR	266	BP 0.03 0.06

The N, E, and Z designations at the beginning of each channel name indicate the north–south, east–west, and vertical components of motion, respectively. *BP* Butterworth band-pass filter, using three poles. Δ epicentral distance

2009); and finally, the model used by the ADSN team to locate earthquakes in the Algiers region, which indicates in our study maximum aftershock locations compared with the results obtained by other tested models. The locations obtained by different velocity models are quite similar (Table 4). With this geometrical distribution of the network, we consider the results of locations as the best that we can obtain with the quantity and quality of data at our disposal. The horizontal and vertical location errors (ERH, ERZ) are 0.58 and 0.40 km for the first event, 0.35 and 0.32 km for the second event, and 0.40 and 0.30 km for the last event, respectively (Table 4). We have constrained the focal depth by computing a waveform modeling for each depth (see the Waveform Modeling and Results sections).

For the aftershocks, among the ten short-period stations, one of them was installed in northern Medea city (AMED) after the first event (Fig. 3) to reinforce the ADSN permanent network. The station operated from 21 August to 25 September 2007. Because the set of data is not very large, we used at least four P-wave and one S-wave reading in order to locate aftershocks. Fifty-eight aftershocks were located (Fig. 3b). The closest stations located in the epicentral area and having recorded a maximum number of aftershocks are EMHD and ATAF (broadband) and AMED, ASID, AABA, ADJB, and AKET (short-period). Twenty-five events with RMS < 0.35, ERH < 2.2 km, and ERZ < 3.3 km were selected and will be discussed in the Discussion and Conclusions section. The duration magnitude is deduced from the coda length of aftershocks. The aftershock duration magnitude *Md* ranges from 1.3 to 3.0.

5. Source Parameter Estimation

5.1. Waveform Modeling

Data processing in FMNEAR includes removing the pre-event baseline offset, manually picking the initial P-wave arrival time, integrating the velocity time series to obtain the displacement, windowing, time shifting, band-pass filtering, and decimation (Delouis, 2014). The first P-wave arrival times were manually picked from vertical records to avoid

Table 6

Velocity model used to generate the synthetic seismograms

Layer thickness (km)	V_p (km/s)	V_s (km/s)	Density (g/cm^3)	Q_p	Q_s
0.60	3.30	1.90	2.00	200.00	100.00
1.40	4.50	2.60	2.30	350.00	175.00
3.00	5.50	3.18	2.50	500.00	250.00
25.00	6.50	3.75	2.90	600.00	300.00
0.00	8.10	4.68	3.30	1000.00	500.00

V_p and V_s; P- and S-wave velocities, respectively. Q_p and Q_s: P- and S-wave quality factors, respectively

introducing errors from both the automated picking algorithm and the FMNEAR method itself. All other aspects of the data processing were automated. Filtering parameters (e.g., minimum and maximum frequencies) can be either manually adapted to each component of the seismic data or determined automatically; here the corner frequencies for the components were between 0.03–0.11 Hz, except for the northern component of the OJGS station which were 0.11–0.17 (Table 5). Removing the high-frequency noise helps constrain the fault orientation and slip direction. The FMNEAR method automatically discards the components whose observed waveforms are poorly fitted by the synthetic waveforms during the inversion (Delouis, 2014).

We tested several velocity models to obtain the optimal fit. We first tested local velocity models that were proposed for the region in previous studies
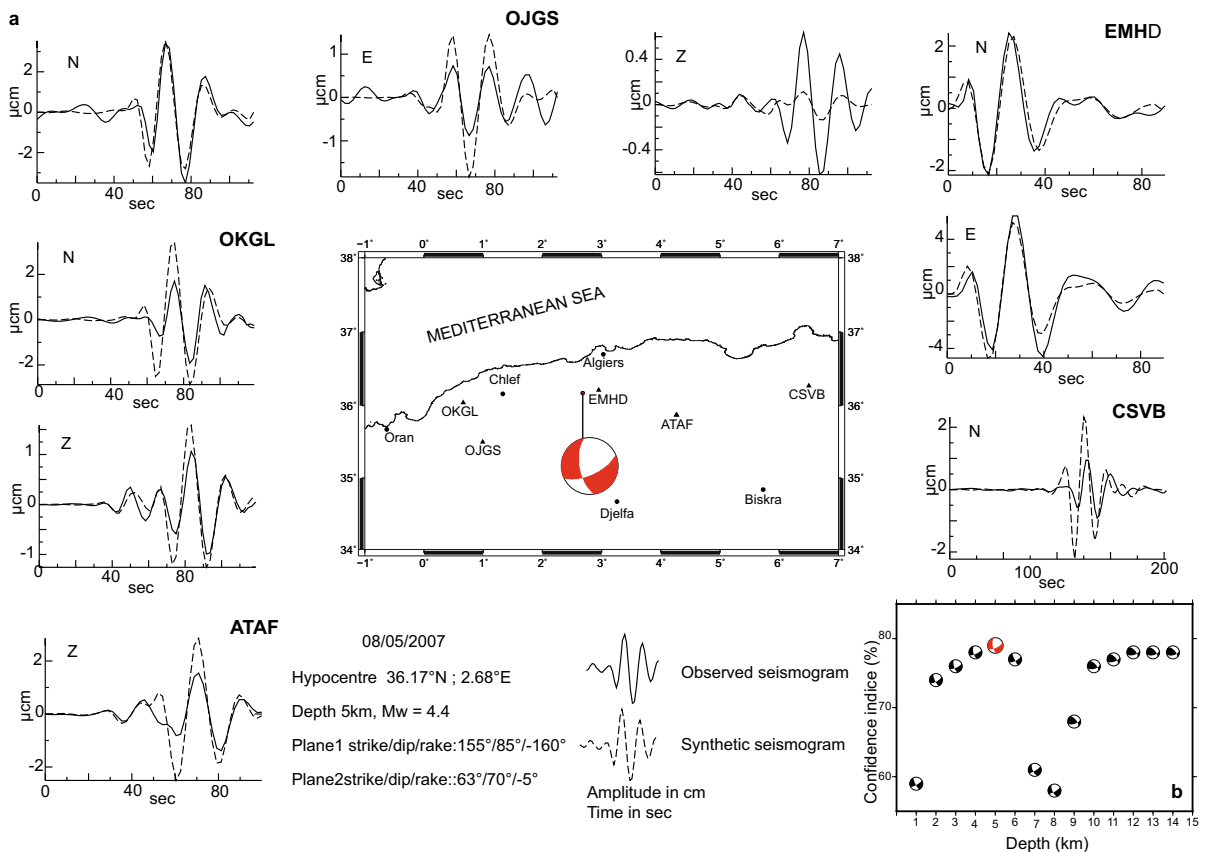

Figure 4

a Waveform inversion results for the first significant earthquake of the sequence, *Mw* 4.4, 08 May 2007, 06:50 UTC. The map shows the focal mechanism. Triangles indicate the broadband stations used to compute the focal mechanism. The best-fit synthetic seismograms (dashed lines) and observed seismograms (continuous lines) are superimposed. **b** Map showing confidence index (CI %) versus depth (km). The red focal mechanism is the best solution (depth = 5 km)
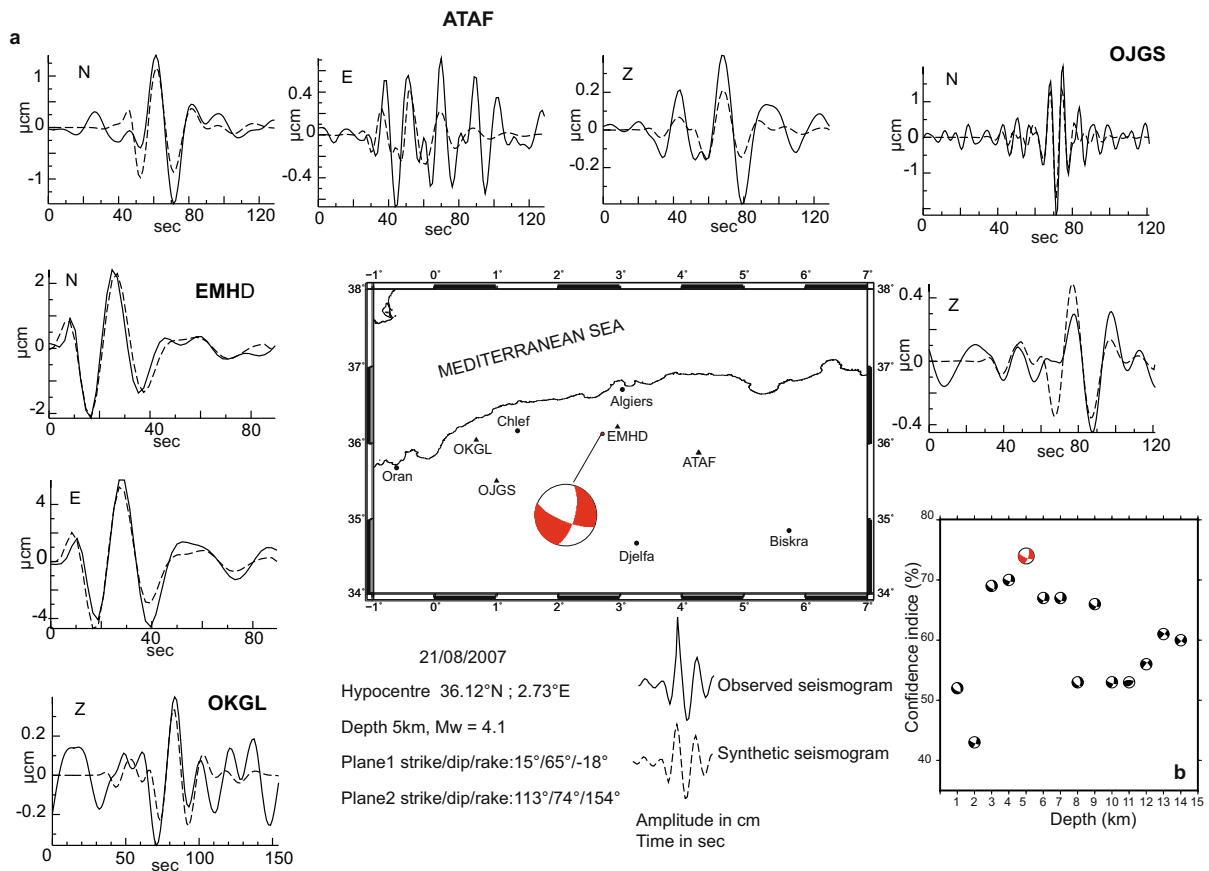
Figure 5

a Waveform inversion results for the second significant earthquake of the sequence, *Mw* 4.1, 21 August 2007, 14:55 UTC. The figure is structured the same as in Fig. 4a. **b** The red focal mechanism is the best solution (depth = 5 km)

(Table 3). However, the best results were obtained with the velocity model proposed by Delouis (Delouis, 2014; Delouis et al., 2009), which corresponds to the default model of the FMNEAR web service (Table 6). This consists of an average crustal model that has been shown to provide reliable results in various geologic settings (Delouis, 2014), and was previously used in Algeria with good results (Beldjoudi et al., 2016; Semmane et al., 2015; Yelles-Chaouche et al., 2017).

We computed earthquake source parameters using the FMNEAR method (Delouis, 2014), which is based on both waveform inversion of near-source broadband or strong-motion seismic records, and a double-couple point-source model. This method involves a combination of simulated annealing over the focal mechanism parameter space (strike, dip, and

rake) and the source-time function. The seismic moment (M_0), and hence moment magnitude (*Mw*), are obtained via integration of the source time function. The best-fit solution minimizes the root-mean-square (RMS) error between the observed and calculated seismograms,

$$RMS = \sqrt{\frac{\sum(obs - cal)}{\sum obs^2}} \qquad (1)$$

where *obs* and *cal* are the observed and calculated waveforms, respectively. The acceleration and velocity waveforms were integrated to compute the displacement waveforms and band-pass-filtered prior to the inversion.

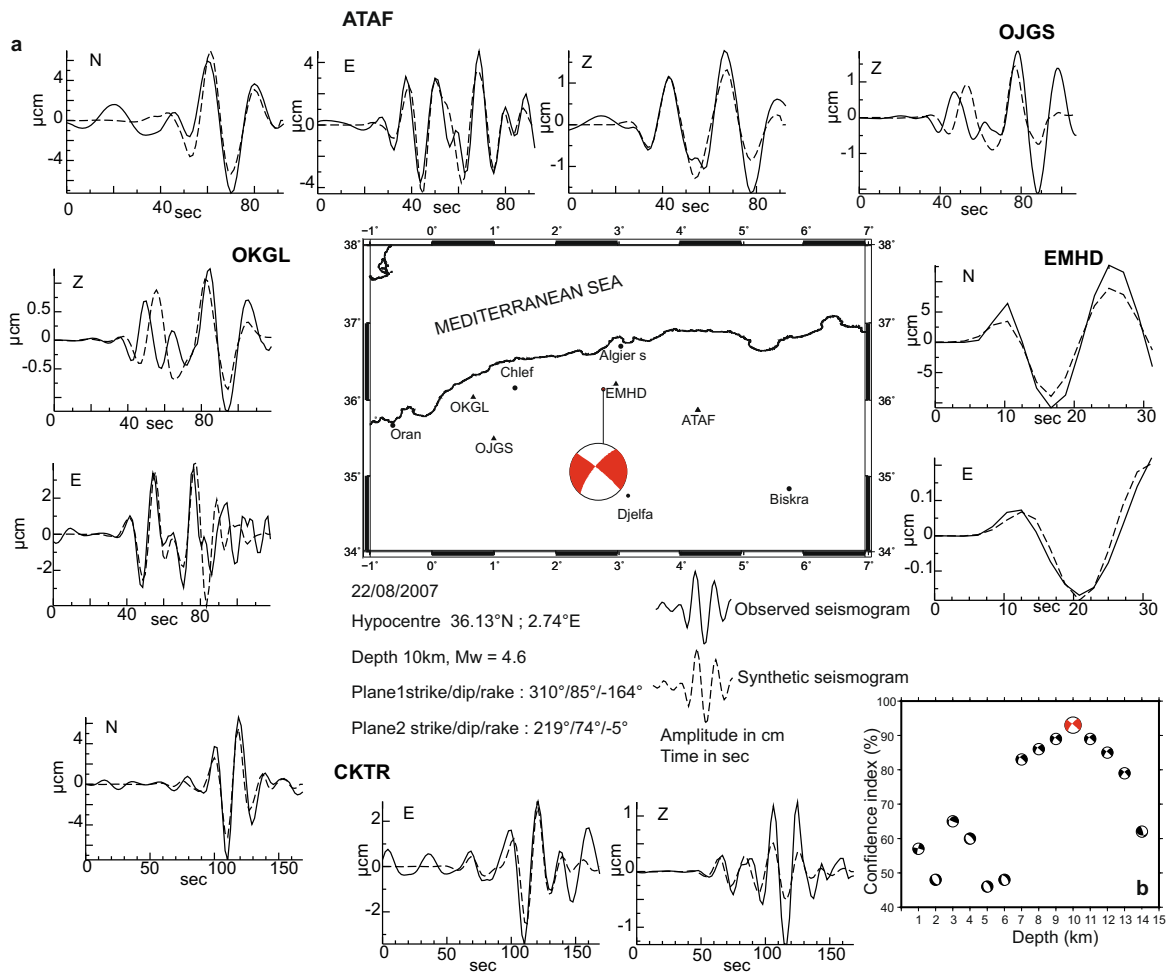A confidence index (*CI*), which varies between 0% (no confidence) and 100% (total confidence),

Figure 6

a Waveform inversion results for the third significant earthquake of the sequence, *Mw* 4.6, 22 August 2007, 18:06 UTC. The figure is structured the same as in Fig. 4a. **b** The red focal mechanism is the best solution (depth = 10 km)

describes the uniqueness and quality of the solution: $CI > 70\%$ represents an acceptable solution (Beldjoudi et al., 2016; Delouis, 2014). The FMNEAR method is not strongly sensitive to the choice of velocity model since it uses relatively low frequencies (typically 0.02–0.10 Hz). The inversion procedure starts with an initial fixed depth that was obtained from the event location. However, it is possible to explore the effects of variations in the fixed parameter values on the solution. To effectively constrain a focal depth, the waveform inversion is done at different hypocentral depths with a step of 1 km.

5.1.1 Results

Five broadband stations were incorporated into the waveform modeling for the first event (Fig. 4a), and nine components were selected to estimate the FM and source parameters. The best-fit solution yielded $RMS = 0.46$ and $CI = 79\%$ at an optimal depth of 5 km. The FM was represented by a NNW–SSE-oriented plane with right-lateral normal movement and NE–SW-oriented plane with left-lateral normal movement. Four broadband stations were incorporated into the inversion procedure for the second event (Fig. 5a), and eight components were used to calculate the FM and source parameters. The best-fit

Table 7

Source parameters obtained in this study for the main events using the waveform inversion and the displacement spectra and those given by INGV (www.ingv.it) and IGN (www.ign.es) for the first and the third events

| Event | Waveform inversion | | | | | | M_w | M_0 (Nm) | Displacement spectra | | Obs. |
| | Plan (1) | | | Plan (2) | | | | | M_w | M_0 (Nm) | |
	Strike (°)	Dip (°)	Rake (°)	Strike (°)	Dip (°)	Rake (°)					
1	63	70	−05	155	85	−160	4.41	4.72e+15	4.41	4.73e+15	This study
	51	83	−19	144	71	−173	4.30	3.60e+15			INGV
	49	79	−15	142	75	−168	4.20	2.58e+15			IGN
2	15	65	−18	113	74	154	4.09	1.55e+15	3.97	1.01e+15	This study
3	219	74	−05	310	85	−164	4.58	8.58e+15	4.57	8.06e+15	This study
	23	67	−30	125	63	−154	4.40	5.70e+15			INGV
	38	28	11	299	85	118	4.40	4.80e+15			IGN

solution yielded $RMS = 0.44$ and $CI = 74\%$ at an optimal depth of 5 km. The FM was represented by a NNE–SSW-oriented plane with left-lateral normal movement and a WNW–ESE-oriented plane with right-lateral normal movement. Five broadband stations were incorporated into the inversion procedure for the third event (Fig. 6a), and 11 components were used to estimate the FM and source parameters. The best-fit solution yielded $RMS = 0.39$ and $CI = 93\%$ at an optimal depth of 10 km. The FM exhibited almost pure strike-slip and consisted of a NE–SW-oriented plane with left-lateral movement and a NW–SE-oriented plane with right-lateral movement. To effectively constrain the focal depth, we calculated source parameters at different hypocentral depth from 1 to 15 km with a step of 1 km. We present depth (km) versus confidence index (CI %) to validate the optimal focal depth solutions. This illustrates the best fits between synthetic and observed seismograms. The selected focal depths are 5 km for the first and the second event (Figs. 4b and 5b) and 10 km for the third one (Fig. 6b).

The moment magnitude was also computed using the FMNEAR method, which is ideal for moderate events when the displacement spectra of the near-field records are available. The spectral amplitudes obtained from the low-frequency real data were compared to the amplitudes from the synthetic records that were computed using kinematic rupture models scaled to M_w (Delouis et al., 2009). The results are presented in Table 7.

5.2. Source Spectrum Modeling

The methodology used to determine the source parameters from the P- and S-wave spectra has been described in several previous works, including detailed discussions in Abacha et al. (2018), Fletcher (1980), Garcıa et al. (2004), García-García et al. (1996), and Hanks & Wyss (1972). The M_0 and corner frequency (f_c) estimations from the ground motion spectra involve the definition of a theoretical model for the source spectrum. A common model is the circular seismic source of Brune (1970, 1971),

$$S'(f) = \Omega_0 \frac{(2f)^2}{1 + \left(\frac{f}{f_c}\right)^2}, \qquad (2)$$

where S' is the displacement amplitude spectra of a P or S wave at frequency f, and Ω_0 is the low-frequency spectral flat level, which is proportional to M_0 in Nm (Keylis-Borok, 2010). The following equations were used to calculate M_0, the stress drop ($\Delta\sigma$), source radius (r), and average displacement (U), respectively:

$$M_0 = \frac{4\pi\rho.V^3\Omega_0}{kR_{(,)}} \qquad (3)$$

$$\Delta = \frac{7M_0}{16r^3} \qquad (4)$$

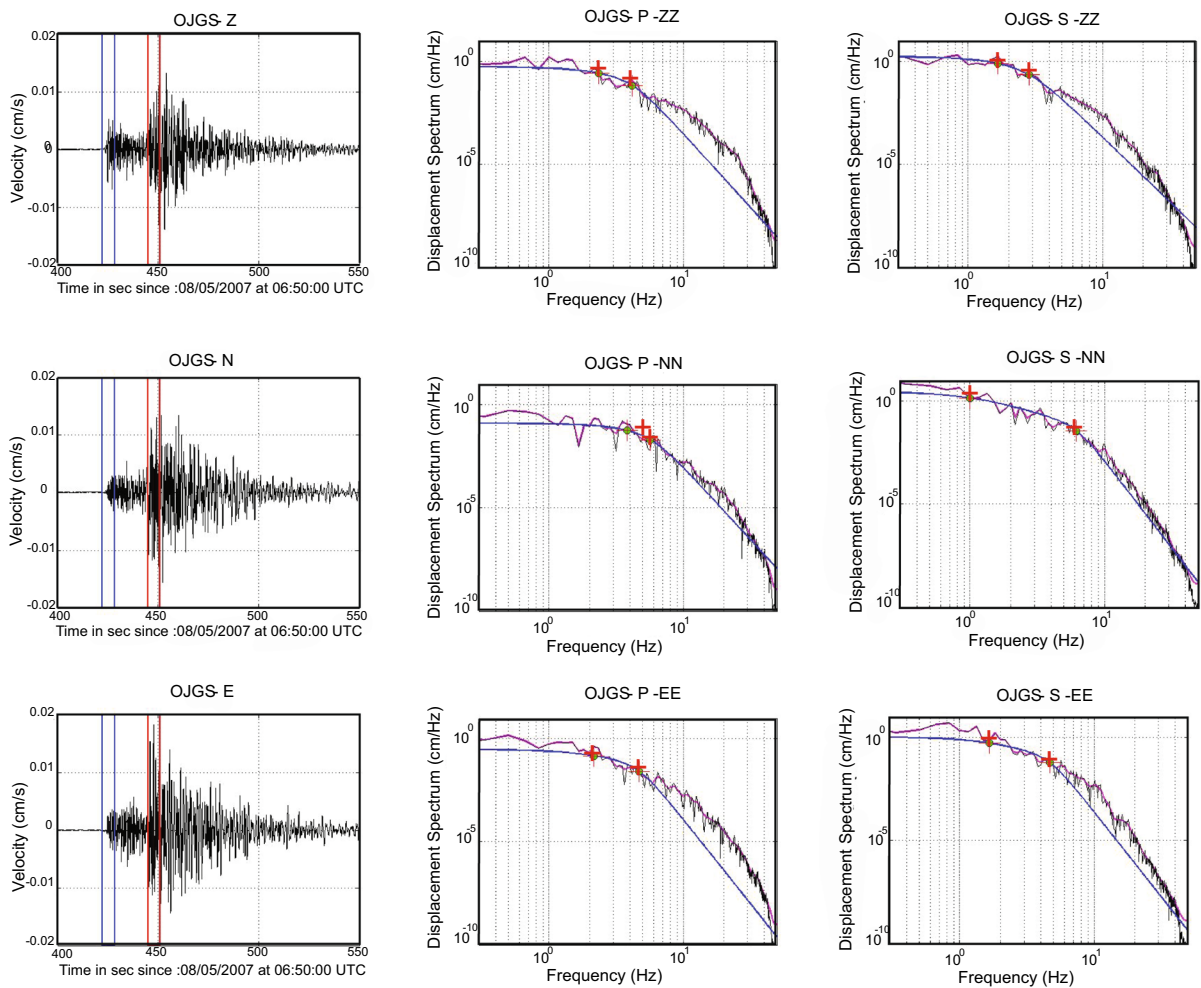$$r = 2.34\frac{V}{2\pi f_c}, \qquad (5)$$

and

Figure 7
Displacement spectra for the 08 May 2007 *Mw* 4.4 event, recorded at station OJGS. Left panel: instrumentally corrected three-component velocity seismograms. Blue and red lines indicate the *P* and *S* onsets, respectively. Middle panel: *P*-wave displacement spectra. Right panel: *S*-wave displacement spectra. Blue lines are the fitted spectra. Red crosses represent the low-frequency plateaus Ω_0 with corner frequencies f_c and maximum frequencies $f_{\max}$

$$U = \frac{M_0}{G\pi r^2} \qquad (6)$$

where ρ is the density of the medium (2.70 g/cm³), Δ is the hypocentral distance, V is the P- or S-wave velocity near the source, Ω_0 is the low-frequency spectral flat level, G is shear modulus (3×10^{10} N/m²), $R_{(\theta,\varphi)}$ is the radiation pattern coefficient, and k is a correction factor for the free surface reflection, which is estimated to be 1.0 here (Aki & Richards, 1980). The moment magnitude (*Mw*) can be calculated from the above equations using the

formula of Hanks and Kanamori (Hanks & Kanamori, 1979; Kanamori, 1977):

$$M_w = \left(\frac{2}{3}\right) \log M_0 - 6.0. \qquad (7)$$

5.2.1 Results

We determined the source parameters from the ground-motion spectra using a routine developed in Abacha et al. (2018) to automatically estimate the spectral displacement parameters, including Ω_0 and
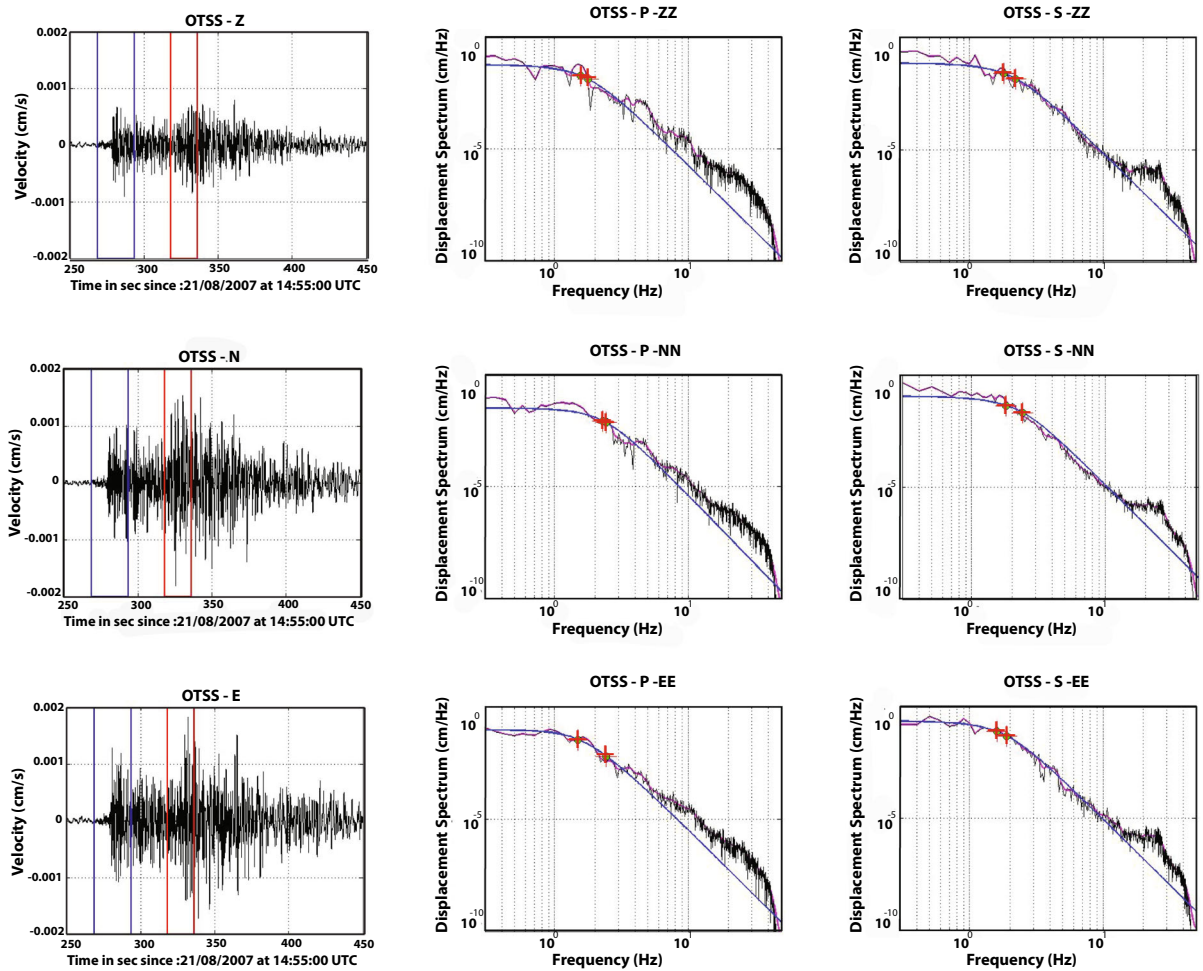
Figure 8

Displacement spectra for the 21 August 2007 *Mw* 4.1 event, recorded at station OTSS. The figure is structured the same as in Fig. 7

f_c, which are based on fitting the displacement spectra in Eq. (2) to the observed spectra. The displacement spectra were corrected for attenuation and smoothed by applying a Konno–Ohmachi log-scale window (Abacha et al. 2018) and then fitted to theoretical spectra (Figs. 7, 8, 9).

Here, we used $R_{(\theta,\varphi)} = 0.52$ for P waves and $R_{(\theta,\varphi)} = 0.63$ for S waves (Abacha et al., 2018; Boore & Boatwright, 1984) to calculate r, M_0, and $\Delta\sigma$ for each of the three largest events in the seismic sequence. The data were analyzed separately in two successive time windows containing the P and S onsets. The calculations were made using the P and S waves separately, as well as combined. The resultant f_c, M_0, r, and Mw values, as well as the multiplicative

error factors for the seismic moment (EM_0) and corner frequency (Ef_c), for each event are listed in Table 8. It should be noted that the components that yielded a poor fit between the theoretical and experimental spectra were excluded. The average values that were obtained from the P- and S-wave data for each event are presented in Table 8. The flat spectral level Ω_0 of the total spectrum is equal to the square root of the sum of squares of each component at the flat levels. The f_c value was averaged over the three components of each station, and the average M_0 (P, S) and f_c (P,S) values were estimated for each event using the formulae of Archuleta (Abacha et al., 2018; Archuleta et al., 1982). The calculated M_0 values ranged from 1.01 to 8.06 × 10^{15} Nm, which
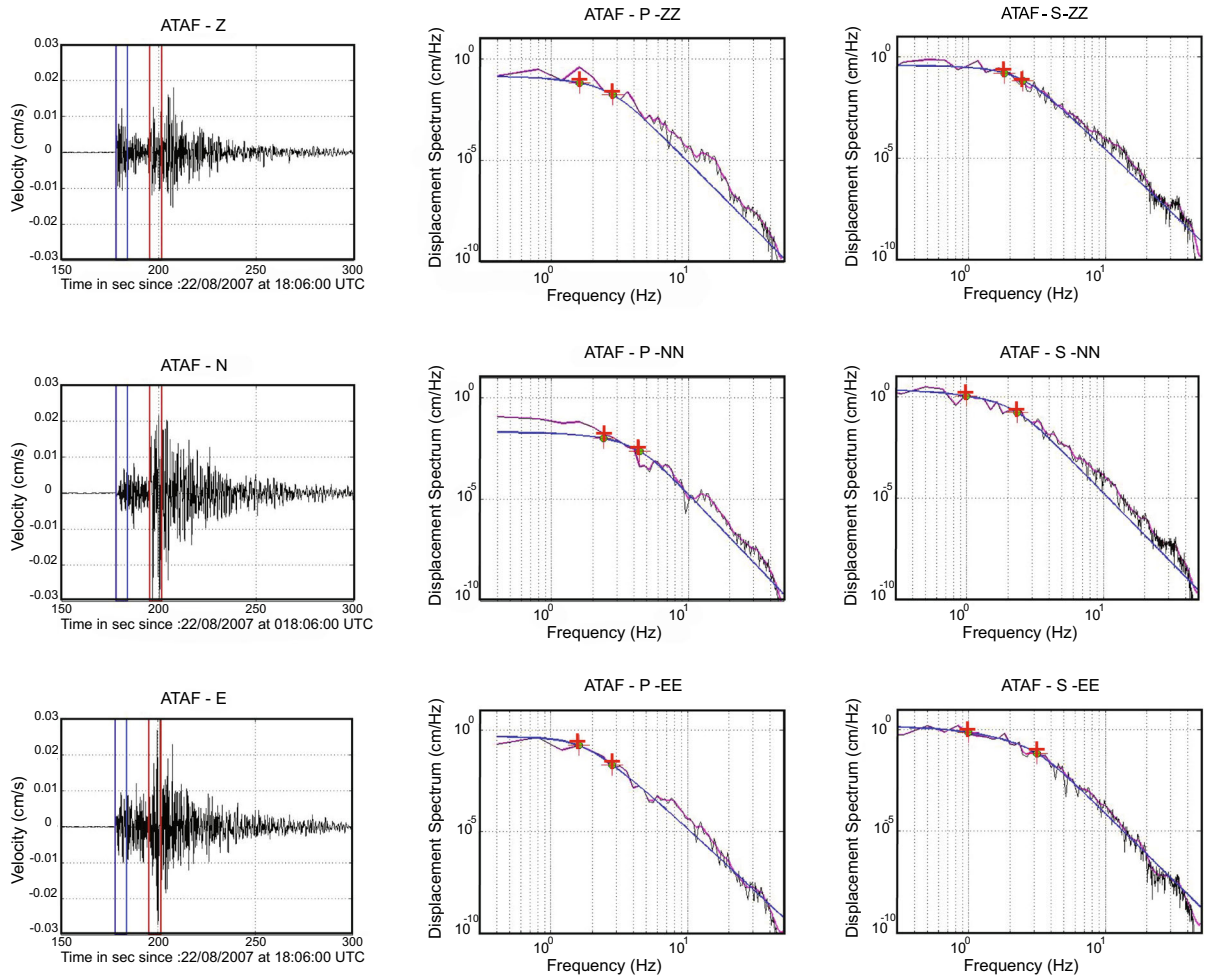
Figure 9
Displacement spectra for the 22 August 2007 *Mw* 4.6 event, recorded at station ATAF. The figure is structured the same as in Fig. 7

correspond to $Mw \sim 4.0$–4.6, $r = 0.85$–1.14 km, $\Delta\sigma = 0.8$–2.4 MPa, and $f_c = 1.8$–2.2 Hz (Table 9). The seismic moments and moment magnitudes of the events are comparable to the FMNEAR inversion results (Table 7).

6. Stress Inversion

We calculated the orientations of the main axes of the stress tensor ellipsoid using the GRID-SIM_STRESS algorithm (Delouis et al., 2002). We used the FMs of the three large events in the Medea seismic sequence (Table 7) and ten focal mechanisms

of earthquakes that occurred in the northern and eastern parts of the Medea region (Table 10) in the stress tensor inversion. The best-fit stress tensor is obtained by minimizing the angular deviation (average scalar product) between the observed and computed slip vectors on the nodal planes of the FMs (Beldjoudi et al., 2009, 2011, 2016; Delouis et al., 2002; Khelif et al., 2018). The best-fit solutions (black circles) indicate that the σ_1 axis is horizontal (plunge 7°) and oriented N335°E, the σ_2 axis is horizontal (plunge = 6°) and oriented N65°E, and the σ_3 axis is nearly vertical (plunge 81°) (Fig. 10). These results are obtained with a score of 0.96, which shows that all of these FMs are highly consistent with

Table 8

Computed values during the source parameter estimation of the main events

	$< f_c >$	Ef_c	$< M_0 >$	EM_0	$< M_w >$	$< r >$
Event 1						
PZ	1.96	1.40	1.00e+16	2.73	4.49	1279
PN	2.17	1.13	5.34e+15	1.46	4.30	999
PE	2.60	1.40	2.08e+16	2.90	4.35	875
PZNE	2.21	1.13	8.07e+15	1.49	4.45	930
SZ	1.68	1.38	2.49e+15	2.11	4.17	783
SN	1.80	1.13	5.22e+15	1.32	4.31	1155
SE	1.92	1.38	5.66e+15	2.17	4.26	786
SZNE	1.53	1.13	4.38e+15	1.34	4.31	856
PSZ	1.82	1.39	6.24e+15	2.42	4.33	1031
PSN	1.98	1.13	5.28e+15	1.39	4.30	1077
PSE	2.26	1.39	1.32e+16	2.54	4.30	830
PSZNE	1.87	1.13	6.22e+15	1.41	4.38	893
Event 2						
PZ	1.97	1.37	1.16e+16	1.87	4.58	1183
PN	2.35	1.12	4.33e+15	1.26	4.22	1556
PE	2.18	1.38	8.78e+15	1.91	4.49	1008
PZNE	2.16	1.13	9.32e+15	1.27	4.54	1034
SZ	1.23	1.35	6.41e+15	1.51	4.35	1170
SN	1.41	1.12	5.65e+15	1.16	4.41	951
SE	1.29	1.35	1.15e+16	1.52	4.62	1342
SZNE	1.31	1.12	8.75e+15	1.17	4.54	985
PSZ	1.60	1.36	9.05e+15	1.69	4.46	1176
PSN	1.88	1.12	4.99e+15	1.21	4.31	1253
PSE	1.73	1.37	1.01e+16	1.71	4.55	1175
PSZNE	1.74	1.12	9.04e+15	1.22	4.54	1010
Event 3						
PZ	2.56	1.65	1.38e+15	1.58	4.01	1255
PN	3.07	1.21	5.55e+14	1.19	3.65	859
PE	2.64	1.68	1.46e+15	1.60	3.99	1022
PZNE	2.76	1.21	1.26e+15	1.19	3.98	923
SZ	1.88	1.43	4.28e+14	1.39	3.65	681
SN	1.78	1.14	1.08e+15	1.13	3.95	881
SE	2.54	1.44	9.06e+14	1.40	3.83	590
SZNE	2.07	1.14	8.83e+14	1.13	3.89	644
PSZ	2.22	1.54	9.07e+14	1.49	3.83	968
PSN	2.43	1.17	8.19e+14	1.16	3.80	870
PSE	2.59	1.56	1.18e+15	1.50	3.91	806
PSZNE	2.41	1.18	1.00e+15	1.16	3.93	784

f_c corner frequency in Hz; M_0 seismic moment in Nm; EM_0 and Ef_c multiplicative error factors for the seismic moment and corner frequency, respectively; Mw moment magnitude; r source radius in meters; *PZ, PN,* and *PE* vertical, northing, and easting components of motion from the *P*-wave data; *PZNE* values averaged over the three *P*-wave components of motion; *SZ, SN,* and *SE* vertical, northing, and easting components from the *S*-wave data; *SZNE* values averaged over the three *S*-wave components of motion

a common stress tensor. We note that the best scores correspond to either the compressional regime (subvertical σ_3 axis) or strike-slip regime (subvertical σ_2 axis) on a score versus shape factor (*C*) diagram. This is related to the possibility that the σ_2 and σ_3 axes occupy similar positions in the stereographic plots; the σ_1 axis is well constrained in this case. The possibility of a strike-slip regime is related to the fact that the three events examined in this study exhibit small normal faulting components, which cannot be explained by a subvertical σ_3 axis.

7. Coulomb Stress Transfer

We attempt to understand the interaction between fault segments by estimating the stress transfer between events. First, we investigate whether the first event (*Mw* 4.4) loaded stress for the second event (*Mw* 4.1). Then, we investigated whether these two events loaded stress for the third event (*Mw* 4.6).

The change in Coulomb stress ΔCFF is given by the relationship

$$\Delta CFF = \Delta \tau + \mu'.\Delta \sigma_n \qquad (8)$$

where $\Delta \tau$ is the shear stress variation, $\Delta \sigma_n$ is the normal stress variation, and μ' is the effective coefficient of friction. We simulate the static stress transfer following the first event of the seismic sequence in an elastic half-space (Okada, 1992) using the Coulomb 3.4 software package (Lin & Stein, 2004; Toda et al., 2005). We assume a shear modulus $\mu = 3.2 \times 10^5$ bar, Poisson's ratio $v = 0.25$, and $\mu' = 0.4$ (Beldjoudi, 2020; Dabouz & Beldjoudi, 2019; Kariche et al., 2017; Khelif et al., 2018; King et al., 1994; Lin et al., 2011; Semmane, 2005). The source parameters that are obtained from waveform modeling of the fault segments are given in Table 11.

7.1. Stress Change Following the First Event

We first calculated ΔCFF at depth $z = 5$ km. We used source fault parameters (strike, dip, rake) of 63°, 70°, −5° for the first event and receiver fault parameters of 15° 65°, −18° for the second event. Figure 11a shows four positive lobes, two at the extremities of the source fault and two in the northwest and southeast segments, including where the receiver fault is located. Other regions show a decrease in ΔCFF. The calculated value below the

Table 9

Average values from the source spectrum modeling (from P and S waves)

Event	$< f_c >$	Ef_c	$< M_o >$	EM_o	$< M_w >$	$< r >$	$< \Delta\sigma >$	$< U >$
1	1.78	1.39	4.73e+15	2.42	4.41	1050	1.77	0.049
2	2.20	1.54	1.01e+15	1.49	3.97	847	0.79	0.015
3	1.66	1.36	8.06e+15	1.69	4.57	1136	2.42	0.066

f_c corner frequency in Hz; M_0 seismic moment in in Nm; r source radius in meters; $\Delta\sigma$ stress drop in MPa; Mw moment magnitude; U displacement in m; EM_0 and Ef_c multiplicative error factors for the seismic moment and corner frequency, respectively

Table 10

Focal mechanisms of significant earthquakes in central Algeria between 1989 and 2016, which were used to compute the regional stress tensor

Event N°	Strike (°)	Plan (1) Dip (°)	Rake (°)	Strike (°)	Plan (2) Dip (°)	Rake (°)
1	246	56	86	73	34	96
2	225	72	88	51	18	96
3	218	75	123	330	36	26
4	54	47	88	237	43	92
5	114	85	174	205	84	5
6	03	40	6	268	86	130
7	84	83	170	175	80	7
8	88	56	130	205	56	42
9	45	45	69	253	49	110
10	171	51	44	50	57	132

epicenter of the second event is ΔCFF = 0.087 bar. We therefore confirmed that the second event was loaded by the first event (Fig. 11).

7.2. Stress Change Following the Second Event

We computed ΔCFF at z = 10 km for two reference μ' values, μ' = 0.4 and 0.1. Our source fault parameters are the planes of the first and second events, and the receiver fault parameters are 219^0, 74^0, and -5^0 for the third event. The receiver fault is located southeast of the first event and northeast of the second event. ΔCFF = 0.003 bar for μ' = 0.4 (Fig. 12a, b), which is well below the earthquake trigger limit of 0.1 bar (King et al., 1994). We decrease μ' to 0.1 to explore the sensitivity to the friction coefficient, which decreases the influence of the normal stress (σ_n) and increases the influence of

the shear stress (τ) on ΔCFF (Fig. 13a, b). We note that ΔCFF increases to 0.007 bar, which is slightly larger than the value obtained for μ' = 0.4, but still below the earthquake trigger limit of King et al. (1994). Therefore, a trigger level of < 0.1 bar may have been sufficient in this case since the third event occurred when ΔCFF was below this critical threshold.

8. Discussion and Conclusions

The Medea region is an active area with moderate earthquakes; no significant events were reported during the historical and instrumental eras. The Medea seismic sequence of May–August 2007 was located southwest of the city of Medea located at the eastern extremity of the Cheliff Basin and occurred on two parallel strike-slip faults (Fig. 14).

Several seismic sequences have been recorded in northern Algeria during the last 20 years, especially in the central part of the Tell Atlas. We quote as an example the 2007 Medea seismic sequence, Hammam-Melouane sequence (Yelles-Chaouche et al., 2017), and Mihoub sequence (Khelif et al., 2018). As mentioned above, the location of this seismic sequence was obtained using a seismic network which does not present an optimal geometrical distribution. To avoid this problem, many velocity models were tested to optimize our locations. We note that the locations with different velocity models are very close and comparable in term of errors (Table 4). International and regional seismological centers have located the three main events (Fig. 1). The epicenters given by the USGS (United States Geological Survey, USA), EMSC (Euro-Med Seismological Center), and IGN (Instituto Geografico
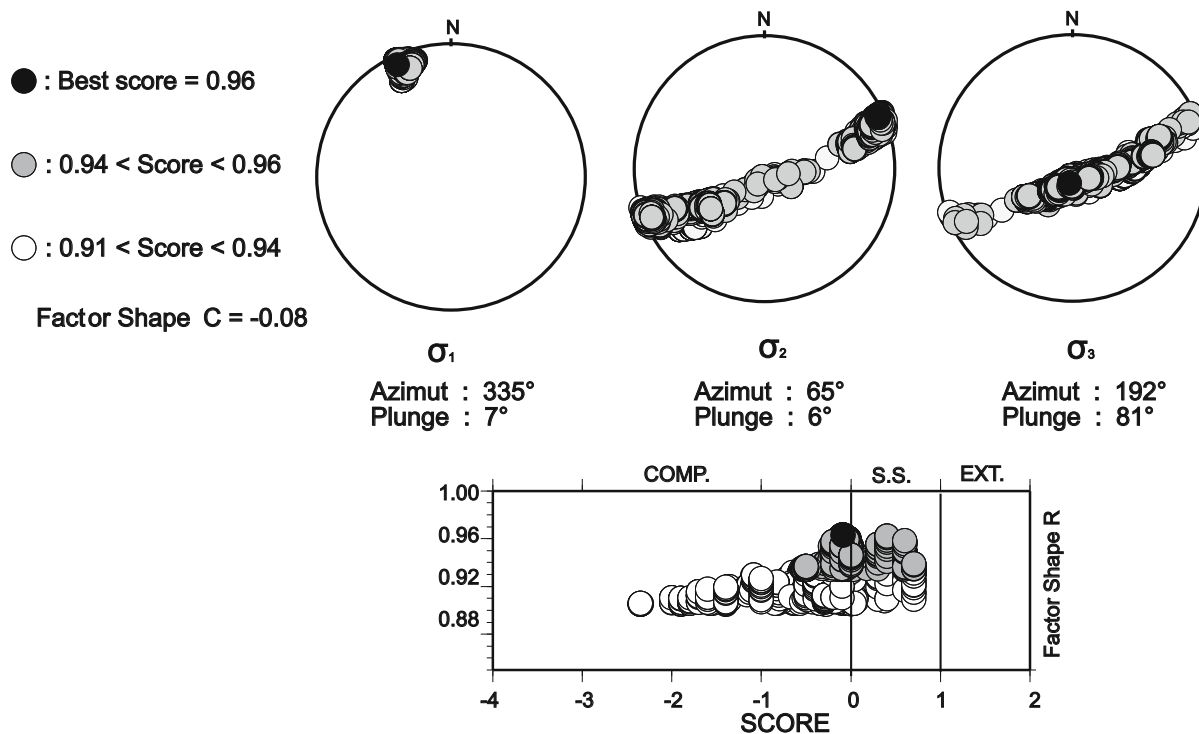
Figure 10

a Solutions for the σ_1, σ_2, and σ_3 axes. The lower-hemisphere equal-area projections are plotted with the azimuth and plunge of the principal stress axes indicated. The best-fit solution (score = 0.96, computed by averaging the scalar products of observed and computed slip vectors) is represented by a black circle. Solutions with slightly degraded scores (0.94–0.96) are indicated by gray circles; we consider these confidence intervals. Solutions with open circles correspond to scores of 0.91–0.94. Plotting a range of solutions provides a graphical representation of the uncertainty in the stress axis orientation and stress shape factor C. **b** Score versus stress shape factor diagram for the principal stress axes. $C = -0.08$, which corresponds to a compressive stress regime (labeled "COMP." in the Figure). "S.S." denotes strike-slip, and "EXT." denotes extensional stress

Nacional) are situated southwest of the epicentral area and are close to our event locations, while, the INGV (Instituto Nazionale di Geofisica e Vulcanologia) has located only two events (the first and the third), the first of which is situated in the southern part of the epicentral area (out of Fig. 1), and the second is in the epicentral area.

Two methods were used to estimate the source parameters: waveform modeling and spectral displacement approaches. The parameters of the seismic sources obtained by these two methods are similar for each event, showing the reliability of our study and the data. We have used the records of broadband seismic stations to compute seismic source parameters of the main events of moment magnitude ranging from 4.1 to 4.6). The FMs were obtained from point-source waveform inversion using the records of five

broadband stations for the first main event and four broadband for the two others events. These broadband stations are located at local and regional distances (Figs. 4, 5, 6). The FMs obtained during this seismic sequence show a strike-slip regime with a left-lateral movement oriented NE–SW for the first plane and a right lateral movement oriented NW–SE for the second plane with a weak normal component. The focal depths of the main events were constrained by computing source parameters at several depths varying between 1 and 15 km (Figs. 4b, 5b, 6b).

Consulting the regional seismological centers like INGV and IGN, they compute only the FMs of the first and the third events. Comparing them to our FMs, their general trends are left-lateral for the planes oriented NE–SW and right-lateral for the planes oriented NW-SE. The parameters of the fault planes

Table 11

Fault parameters used to calculate the Coulomb stress change ΔCFF

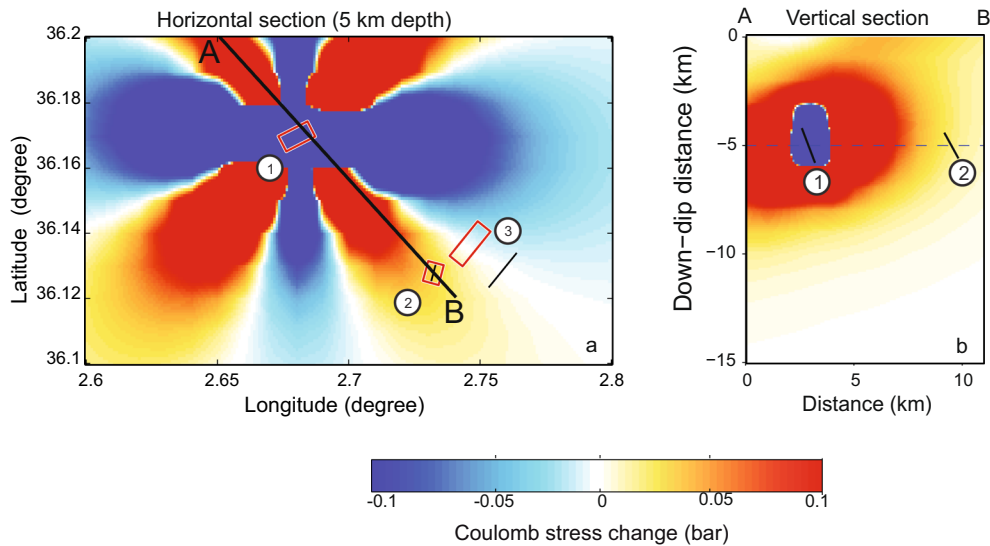| Event	Seismic source (°)			Seismic moment (Nm)	Length (km)	Width (km)	Reverse slip (m)	Right lateral slip (m)	Total slip (m)
	Strike	Dip	Rake						
1	63	70	−5	4.7×10^{15}	1.11	1.70	−0.007	−0.078	0.078
2	15	65	−18	1.7×10^{15}	0.70	1.31	−0.018	−0.054	0.057
3	219	74	−5	9.4×10^{15}	2.04	1.52	−0.008	−0.094	0.094

Figure 11

Change in Coulomb stress (*ΔCFF*) due to source fault 1 (strike 65°, dip 77°, rake −5°) on receiver fault 2 (strike 15°, dip 65°, rake −18°) for friction coefficient μ′ = 0.4. Blue indicates a decrease in stress; red and yellow indicate increases in stress. **a** Horizontal (plan view) plot computed at 5 km depth. Red rectangles represent a horizontal projection of all of the fault segments. **b** Cross-section A–B from a. 1 and 2 indicate the source and receiver faults, respectively

(strike, dip, and rake) are very close for both events (Table 7). The moment magnitudes computed in this work are also very close to those computed by the INGV and IGN; they vary within 0.2. The FM of the second event was not calculated by any seismic centers. We note that USGS gave *Mw* 4.4 for the second event (Table 1). If we compare also the source parameters obtained by displacement spectra and waveform inversion, we find similar results. The M_0 and M_w values computed by the spectral amplitude and FMNEAR methods are similar, demonstrating the reliability of the present study (Table 7).

During our geological field investigation, other nearby seismogenic faults were observed, and are shown in Fig. 14. The contact Miocene deposits and Cretaceous substratum in the northern Bouaichoun area correspond to an 8-km-long, N62°E-oriented, en echelon fault. The contact seems to be an active structure parallel to the Ouzera Fault Zone; we call this segment the Bouaichoun Fault (Fig. 14). Slightly to the southeast, an approximately 7-km-long, N20°E-oriented fault concretizes the contact between the lower part of the Miocene deposits and Cretaceous substratum, which we designate as the Rafsah Fault (Fig. 14).

To plot the main events on the geological map, we note the first event occurred near the NE–SW-trending en echelon Bouaichoun Fault (Fig. 14), which
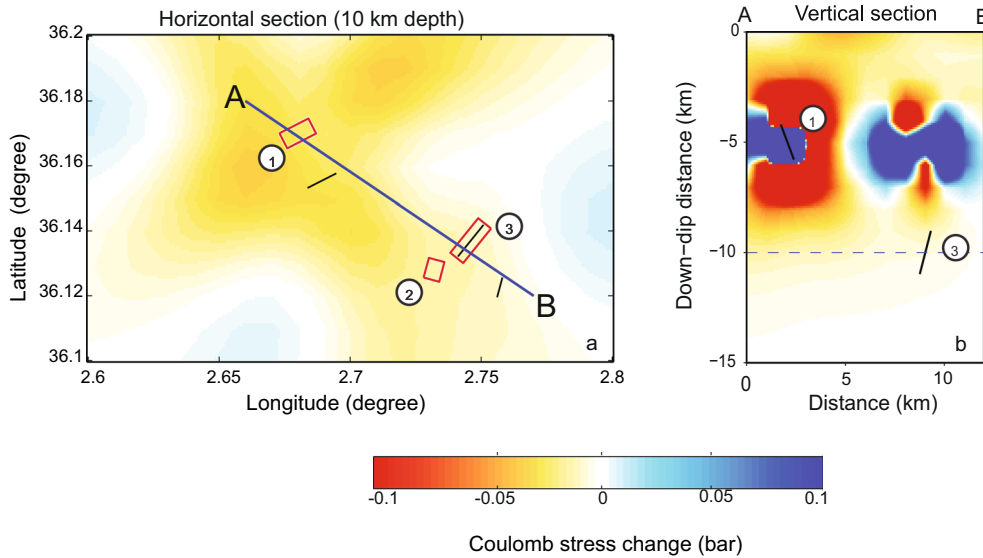
Figure 12

ΔCFF due to source faults 1 and 2 (strike 15°, dip 65°, rake −18°) on receiver fault 3 (strike 219°, dip 74°, rake −5°) for μ′ = 0.4. Blue indicates a decrease in stress; red and yellow indicate increases in stress. **a** Horizontal section (plan view) computed for μ′ = 0.4 at 10 km depth. **b** Vertical cross-section A–B in a shows variations in *ΔCFF* with depth. The source fault here comprises the combined contributions of faults 1 and 2 (not plotted in the figure). Fault 3 is the receiver fault
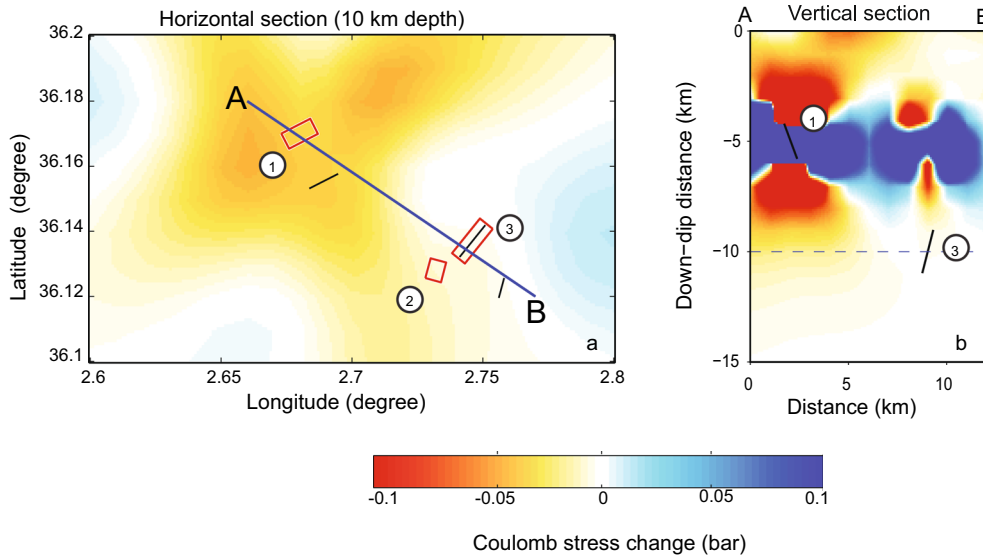

Figure 13

ΔCFF due to source faults 1 and 2 on receiver fault 3 for μ′ = 0.1. The figure is structured the same as in Fig. 12

appears to be a continuation of the Ouzera Fault to the southwest. The FM obtained via waveform modeling indicates a NE–SW-oriented fault plane solution. The strike, dip, and rake of 63°, 70°, and

−5° correspond to the N50°E-aligned fault segment that coincide with the orientation of the Bouaichoun segment (Fig. 14). We confirm this structure is an active one. The FM of the second event presents a
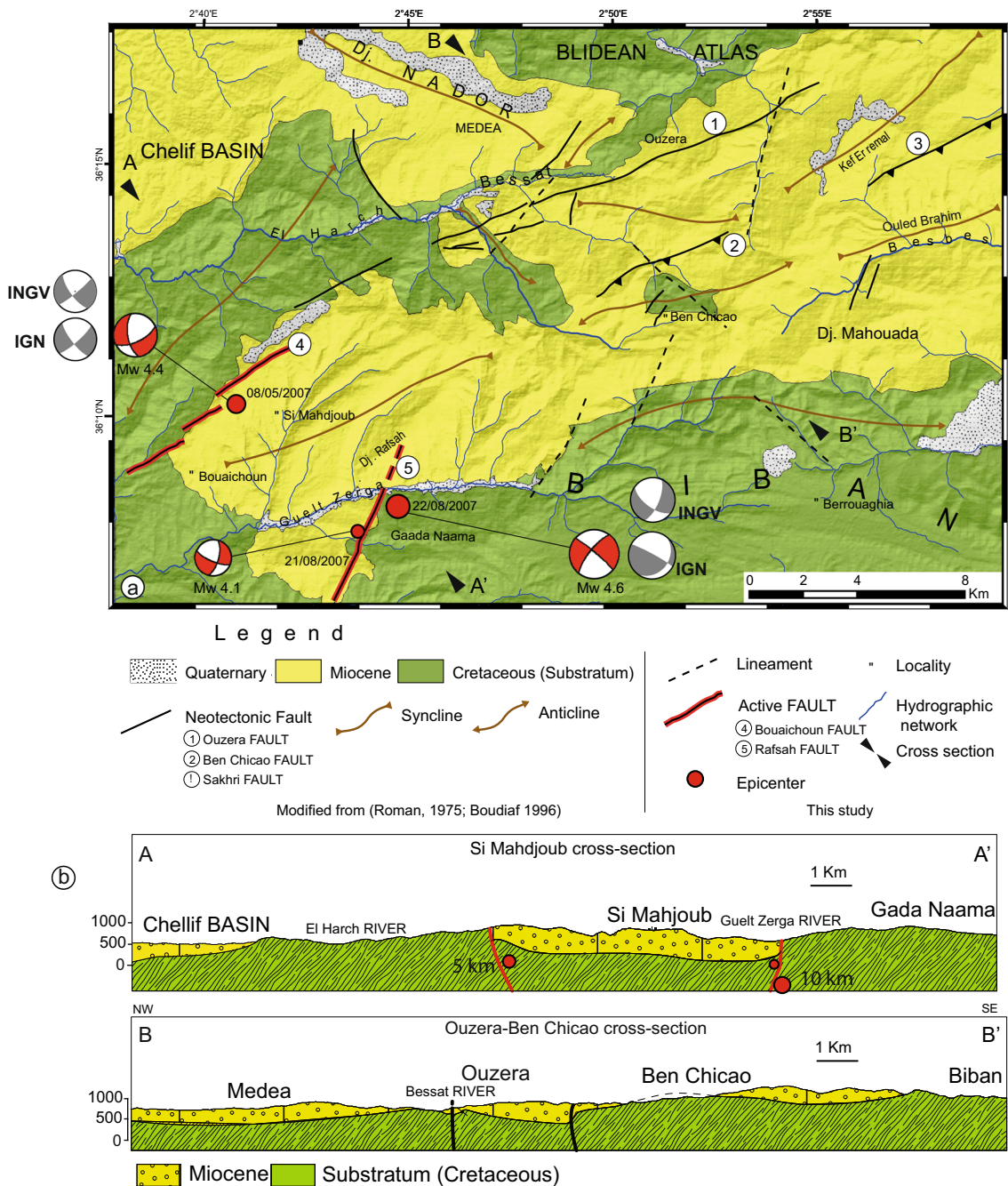
Figure 14

a Same as Fig. 2b. The red focal mechanisms are those of the main events obtained in this study. Grey focal mechanisms are given by international seismologic centers (IGN and INGV) for the first and the third events. **b** NW–SE geological cross-sections: Si Mahdjoub, *A–A'*; Ouzera-Ben Chicao, *B–B'*. Red circles plotted in cross-section *A–A'* are an approximate presentation of the main events

NNE–SSW-oriented nodal plane with left-lateral motion, which can be associated with the identified Rafsah fault (Fig. 14). Waveform modeling resolves a fault-plane strike, dip, and rake of 219°, 74°, and −5°, respectively, for the third event that is associated with left-lateral movement.
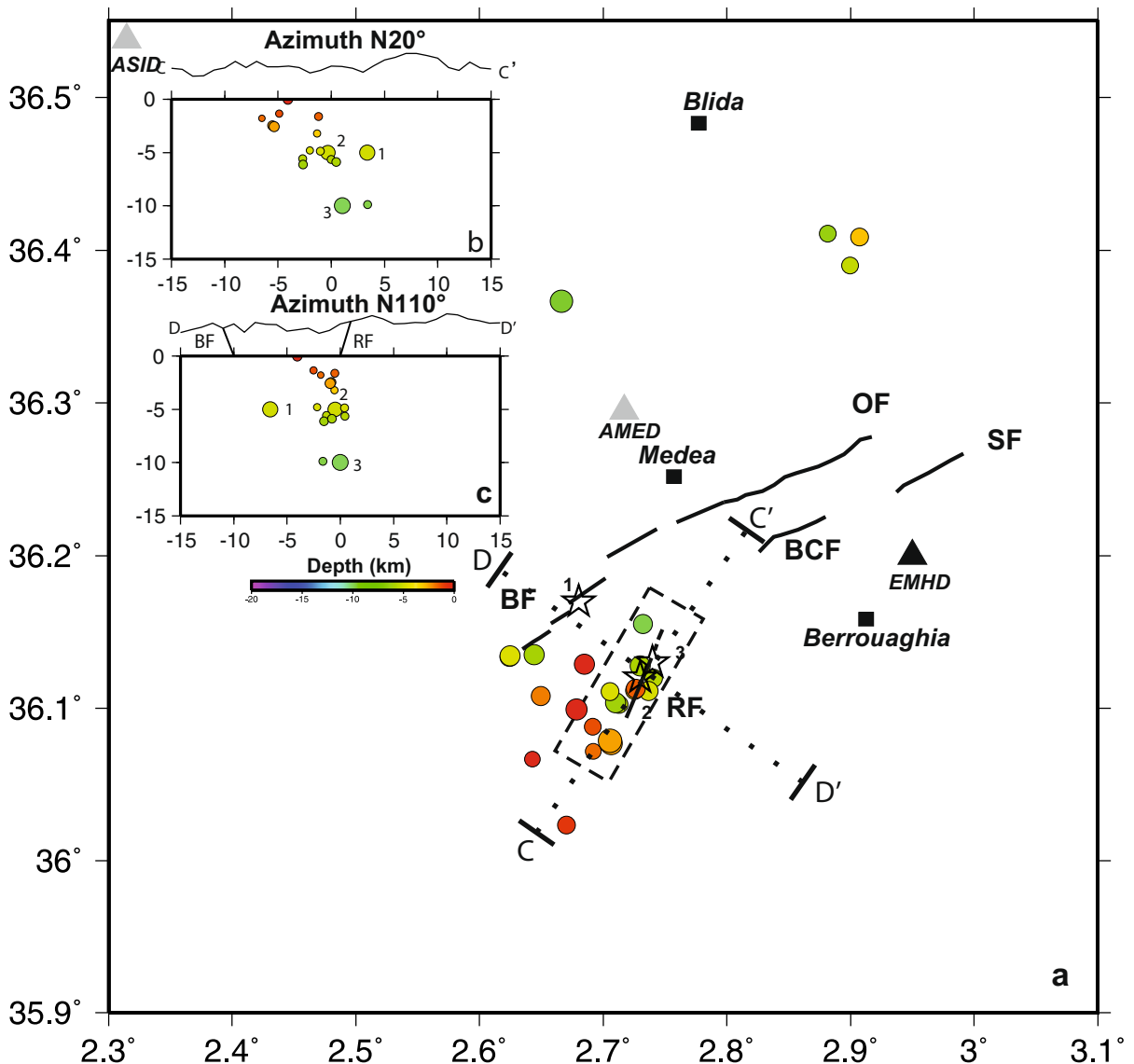
Figure 15

a Aftershock locations of the 2007 seismic sequence. BF: Bouaichoun Fault; OF: Ouzera Fault; SF: Sakhri Fault; BCF: Ben Chicao Fault. Stars 1, 2, and 3 correspond to the three main earthquakes. AMED is the temporary station installed in Medea. The dashed box shows the boundaries of the aftershocks plotted in cross-sections *C–C'* and *D–D'*. **b** Cross-section showing the aftershock locations along a N20°E azimuth. **c** As **b**, but along a N110°E azimuth

After the first event, we did not record any aftershock activity; however, we started to record aftershocks on 21 August. Unfortunately, at this point, we could not install a temporary seismic network to effectively constrain this seismic sequence. We have used the records of the permanent seismic stations which did not cover favorably the epicentral area. Therefore, only 25 of them were selected following the criteria cited in Sect. 4. The aftershocks selected are located within an ∼20-km-long, N20°E-oriented, elongate distribution along the Rafsah Fault (Fig. 15). We select only the aftershocks located inside the dashed box in Fig. 15 and plot them in cross-sections that are rotated to the N20°E and

N110°E azimuths to illustrate this collinearity with the Rafsah Fault (Fig. 15a). The distribution of the hypocenters reveals that the aftershocks roughly match the expected geometry of the Rafsah Fault at depth, trending ~N20°E over a 20 km extent and aligning subvertically at 0–10 km depth. The vertical cross-sections show that most hypocenters are located at 5.0–10.0 km depth. The planar extent of the events in cross-section C–C' is ~13 km (Fig. 15b), and the perpendicular cross-section D–D' outlines a subvertical fault segment, which can correspond to the Rafsah Fault (Fig. 15c).

The stress regime computed for the Medea region is either strike-slip or compressional, depending on whether the axis closer to the vertical is σ_2 or σ_3 (Fig. 10). The ambiguity is related to the existence of normal faulting components for the three events, which tends to promote a stress tensor solution with a vertical component σ_2 (strike-slip regime). The most compressive axis σ_1 found by the stress inversion is well constrained to be near horizontal trending N335°. The trend is almost identical to the values founded in the north of Algeria (Beldjoudi et al., 2009, 2011, 2016; Soumaya et al., 2018).

We conclude that the first event triggered the second event based on estimations of the stress state after each event. The association of the first and second events may have contributed to stress loading and led to the last event; we find a positive but low ΔCFF (<< 0.1 bar), even when computed with $\mu' = 0.1$.

The 2007 sequence demonstrates that active faults persist in the epicentral area, which is marked by NNW–SSE shortening at ~5 mm/year (Bougrine et al., 2019; Calais et al., 2002; Palano et al., 2015; Sella et al., 2002). The Medea region experiences moderate seismicity at a low seismicity rate. We have identified two faults that are related to three significant events in this sequence. The 8-km-long en echelon Bouaichoun Fault may be a southwestward extension of the Ouzera Fault; if so, a full rupture of both segments would result in a $Mw \sim 5.7$ earthquake. The ~20-km-long Ouzera Fault can be considered to possess the greatest seismic hazard in the region, capable of producing an earthquake with a maximum estimated magnitude of Mw 6.3. The 6-km-long, N20°E-oriented Rafsah Fault appears to be a

continuation of the Ben Chicao Fault to the southwest. This subvertical fault can generate $Mw \sim 5.5$ event. The fault characterization in the present study can assist in improving earthquake hazard assessment in the Medea region, whose seismicity remains unstudied.

This study reinforces all geological studies conducted in the Medea region and its surrounding area, and provides new seismotectonic information and some clarification. The most important is the presence of active faults that are principally oriented ~ NE–SW, which can generate moderate earthquakes. In the north part of these faults, we report the presence of large seismogenic structures such as the south border Mitidja basin fault, Mont Chenoua fault, Anticline Sahel fault, and Boumerdes-Zemmouri fault which present a high potential of seismic activity and can generate events with moment magnitude higher than 6.0 (Fig. 1). We want to specify that for this study, we did not have the best geometrical configuration of the network in order to better constrain the seismic sequence. By using the constraint, we were able to determine the parameters of the seismic source by exploiting reliable broadband recordings which have reliable results.

Publisher's Note   Springer Nature remains neutral with regard to jurisdictional claims in published maps and institutional affiliations.

References

Abacha, I., Boulahia, O., Yelles-Chaouche, A., Semmane, F., Beldjoudi, H., & Bendjama, H. (2018). The 2010 Beni-Ilmane,

Algeria, earthquake sequence: Statistical analysis, source parameters, and scaling relationships. *Journal of Seismology, 23*(1), 181–193.

Aki, K., & Richards, P. G. (1980). *Quantitative seismology (2 volumes)*. Freeman and Co.

Archuleta, R. J., Cranswick, E., Mueller, C., & Spudich, P. (1982). Source parameters of the 1980 Mammoth Lakes, California, earthquake sequence. *Journal of Geophysical Research: Solid Earth, 87*(B6), 4595–4607.

Ayadi, A., Maouche, S., Harbi, A., Meghraoui, M., Beldjoudi, H., Oussadou, F., et al. (2003). Strong Algerian earthquake strikes near capital city. *EOS Transactions American Geophysical Union, 84*(50), 5618. https://doi.org/10.1029/2003EO500002

Beldjoudi, H. (2017). Modélisation de la source des séismes par inversion des données sismologiques et géodésiques: application aux séismes du Nord de l'Algérie. Thèse de docorat. Université Côte d'Azur, p. 219.

Beldjoudi, H. (2020). Fault interaction for the Beni-Ilmane (east of Algeria) seismic sequence on May 2010. *Arabian Journal of Geosciences, 13*(18), 1–10.

Beldjoudi, H., Delouis, B., Djellit, H., Yelles-Chaouche, A., Gharbi, S., & Abacha, I. (2016). The Beni-Ilmane (Algeria) seismic sequence of May 2010: Seismic sources and stress tensor calculations. *Tectonophysics, 670*, 101–114.

Beldjoudi, H., Delouis, B., Heddar, A., Nouar, O., & Yelles-Chaouche, A. (2011). The Tadjena earthquake (Mw= 5.0) of December 16, 2006 in the Cheliff region (northern Algeria): Waveform modelling, regional stresses, and relation with the Boukadir fault. *Pure and Applied Geophysics, 169*(4), 677–691.

Beldjoudi, H., Guemache, M., Kherroubi, A., Semmane, F., Yelles-Chaouche, A., Djellit, H., et al. (2009). The Lâalam (Béjaïa, north-east Algeria) moderate earthquake (M w= 5.2) on March 20, 2006. *Pure and Applied Geophysics, 166*(4), 623–640.

Boore, D. M., & Boatwright, J. (1984). Average body-wave radiation coefficients. *Bulletin of the Seismological Society of America, 74*(5), 1615–1621.

Boudiaf, A. (1996). Etude sismotectonique de la région d'Alger et de la Kabylie (Algérie): utilisation des modèles numériques de terrains (MNT) et de la télédétection pour la reconnaissance des structures tectoniques actives: contribution à l'évaluation de l'aléa sismique. Thèse de doctorat de l'Université de Montpellier II, p. 274.

Bougrine, A., Yelles-Chaouche, A. K., & Calais, E. (2019). Active deformation in Algeria from continuous GPS measurements. *Geophysical Journal International, 217*(1), 572–588.

Bounif, A., Bezzeghoud, M., Dorbath, L., Legrand, D., Deschamps, A., Rivera, L., et al. (2003). Seismic source study of the 1989, October 29, Chenoua (Algeria) earthquake from aftershocks, broad-band and strong ground motion records. *Annals of Geophysics, 46*, 625–646.

Bounif, A., Dorbath, C., Ayadi, A., Meghraoui, M., Beldjoudi, H., Laouami, N., et al. (2004). The 21 May 2003 Zemmouri (Algeria) earthquake Mw 6.8: Relocation and aftershock sequence analysis. *Geophysical Research Letters, 31*(19).

Brune, J. N. (1970). Tectonic stress and the spectra of seismic shear waves from earthquakes. *Journal of Geophysical Research, 75*(26), 4997–5009.

Brune, J. N. (1971). Seismic sources, fault plane studies and tectonics. *Eos, Transactions American Geophysical Union, 52*(5), IUDD178–IUDD187.

Caire, A. (1957). Etudes géologiques de la région des Biban. Publ. Serv. Carte géol. Algérie. N.S., Bull. N° 16, voL 2, 1957, p. 818.

Calais, E., DeMets, C., & Nocquet, J.-M. (2003). Evidence for a post-3.16-Ma change in Nubia–Eurasia–North America plate motions? *Earth and Planetary Science Letters, 216*(1–2), 81–92.

Calais, E., Nocquet, J.-M., Jouanne, F., & Tardy, M. (2002). Current strain regime in the Western Alps from continuous Global Positioning System measurements, 1996–2001. *Geology, 30*(7), 651–654.

Dabouz, G., & Beldjoudi, H. (2019). Interaction faults in the northwest of the Mitidja Basin: Chenoua–Tipasa–Ain Benian earthquakes (1989–1996). *On significant applications of geophysical methods* (pp. 261–263). Springer.

Delouis, B. (2014). FMNEAR: Determination of focal mechanism and first estimate of rupture directivity using near-source records and a linear distribution of point sources. *Bulletin of the Seismological Society of America, 104*(3), 1479–1500.

Delouis, B., Déverchère, J., Melnikova, V., Radziminovitch, N., Loncke, L., Larroque, C., et al. (2002). A reappraisal of the 1950 (Mw 6.9) Mondy earthquake, Siberia, and its relationship to the strain pattern at the south-western end of the Baikal rift zone. *Terra Nova, 14*(6), 491–500.

Delouis, B., Pardo, M., Legrand, D., & Monfret, T. (2009). The M w 7.7 Tocopilla earthquake of 14 November 2007 at the southern edge of the northern Chile seismic gap: Rupture in the deep part of the coupled plate interface. *Bulletin of the Seismological Society of America, 99*(1), 87–94.

Domzig, A., Yelles, A. K., Le Roy, C., Dè Verchère, J., Bouillin, J. P., Bracene, R., et al. (2006). Searching for the Africa-Eurasia Miocene boundary offshore western Algeria (MARADJA'03 cruise). *Comptes Rendus Geoscience, 338*, 80–91.

Durand-Delga, M., Didon, J., Foucault, A., & Paquet, J. (1970). Dorsale Bétique. *Annals De La Societe Géologique Du Nord, 90*(4), 382–384.

Fletcher, J. (1980). Spectra from high-dynamic range digital recordings of Oroville, California aftershocks and their source parameters. *Bulletin of the Seismological Society of America, 70*(3), 735–755.

Garcıa, J. G., Romacho, M., & Jiménez, A. (2004). Determination of near-surface attenuation, with κ parameter, to obtain the seismic moment, stress drop, source dimension and seismic energy for microearthquakes in the Granada Basin (Southern Spain). *Physics of the Earth and Planetary Interiors, 141*(1), 9–26.

García-García, J., Vidal, F., Romacho, M., Martín-Marfil, J., Posadas, A., & Luzón, F. (1996). Seismic source parameters for microearthquakes of the Granada basin (southern Spain). *Tectonophysics, 261*(1–3), 51–66.

Guiraud, R. (1977). Sur la néotectonique des régions ouest-constantinoises. *Bulletin De La Société Géologique De France, 7*(3), 645–650.

Hanks, T. C., & Kanamori, H. (1979). A moment magnitude scale. *Journal of Geophysical Research, 84*(B5), 2348–2350.

Hanks, T. C., & Wyss, M. (1972). The use of body-wave spectra in the determination of seismic-source parameters. *Bulletin of the Seismological Society of America, 62*(2), 561–589.

Kanamori, H. (1977). The energy release in great earthquakes. *Journal of Geophysical Research, 82*(20), 2981–2987.

Kariche, J., Meghraoui, M., Ayadi, A., & Boughacha, M. S. (2017). Stress Change and Fault Interaction from a Two Century-Long Earthquake Sequence in the Central Tell Atlas, AlgeriaStress

Change and Fault Interaction from a Two Century-Long Earthquake Sequence. *Bulletin of the Seismological Society of America, 107*(6), 2624–2635. https://doi.org/10.1785/0120170041

Keylis-Borok, V. (2010). On estimation of the displacement in an earthquake source and of source dimensions. *Annals of Geophysics, 53*(1), 17–20.

Khelif, M., Yelles-Chaouche, A., Benaissa, Z., Semmane, F., Beldjoudi, H., Haned, A., et al. (2018). The 2016 Mihoub (north-central Algeria) earthquake sequence: Seismological and tectonic aspects. *Tectonophysics, 736*, 62–74.

Kieken, M. (1974). Étude géologique du Hodna, du Titteri et de la partie occidentale des Biban (Départ. d'Alger, Algérie). *Publ. Serv. géol. Algérie, Nouv. Sér. Bull, 46*.

King, G. C., Stein, R. S., & Lin, J. (1994). Static stress changes and the triggering of earthquakes. *Bulletin of the Seismological Society of America, 84*(3), 935–953.

Klein, F. W. (1978). *Hypocenter location program HYPOINVERSE: Part I. Users guide to versions 1, 2, 3, and 4. Part II. Source listings and notes* (No. 78–694). US Geological Survey.

Lin, J., & Stein, R. S. (2004). Stress triggering in thrust and subduction earthquakes and stress interaction between the southern San Andreas and nearby thrust and strike-slip faults. *Journal of Geophysical Research, 109*, B02303. https://doi.org/10.1029/2003JB002607.

Lin, J., Stein, R. S., Meghraoui, M., Toda, S., Ayadi, A., Dorbath, C., et al. (2011). Stress transfer among en echelon and opposing thrusts and tear faults: triggering caused by the 2003 Mw = 6.9 Zemmouri, Algeria, earthquake. *Journal of Geophysical Research, 116*, B03305. https://doi.org/10.1029/2010JB007654.

Maouche, S., Bouhadad, Y., Harbi, A., Rouchiche, Y., Ousadou, F., & Ayadi, A. (2019). Active tectonics and seismic hazard in the Tell Atlas (Northern Algeria): a review. *The geology of the Arab world––an overview* (pp. 381–400). Springer.

Meghraoui, M. (1988). Géologie des zones sismiques du Nord de l'Algérie: Paléosismologie, tectonique active et synthèse sismotectonique. Thèse de doctorat Paris 11, p. 356.

Meghraoui, M., & Pondrelli, S. (2012). Active faulting and transpression tectonics along the plate boundary in North Africa. *Annals of Geophysics, 55*(5).

Mokrane, A., Ait Messaoud, A., Sebai, A., Menia, N., Ayadi, A., Bezzeghoud, M., et al. (1994). Les séismes en Algérie de 1365 à 1992. Publication du Centre de Recherche en Astronomie, Astrophysique et Géophysique, Département: Etudes et Surveillance Sismique, ESS, CRAAG, Alger-Bouzaréah, p. 277.

Nocquet, J.-M., & Calais, E. (2004). Geodetic measurements of crustal deformation in the Western Mediterranean and Europe. *Pure and Applied Geophysics, 161*(3), 661–681.

Okada, Y. (1992). Internal deformation due to shear and tensile faults in a half-space. *Bulletin of the Seismological Society of America, 82*(2), 1018–1040.

Palano, M., González, P. J., & Fernández, J. (2015). The Diffuse Plate boundary of Nubia and Iberia in the Western Mediterranean: Crustal deformation evidence for viscous coupling and fragmented lithosphere. *Earth and Planetary Science Letters, 430*, 439–447.

Roman, J. C. (1975). Etude géologique du bassin néogène de Médéa (Algérie). Thèse de doctorat de 3ème cycle- Université de Nice.

Rothé, J.-P., Dechevoy, N., & Seltzer, P. (1950). Les séismes de Kerrata et la séismicité de l'Algérie: Pauc.

Sebaï, A. (1997). Analyse sismologique des séismes récents du Sahel d'Alger, Magister Thesis, IST-USTHB, Alger, 178 pp.

Sella, G. F., Dixon, T. H., & Mao, A. (2002). REVEL: A model for recent plate velocities from space geodesy. *Journal of Geophysical Research, 107*(B4), ETG11-11-ETG11-30.

Semmane, F. (2005). *Caractérisation de la source sismique à partir des données en champ proche*. Université Joseph-Fourier-Grenoble I.

Semmane, F., Benabdeloued, B., Beldjoudi, H., & Yelles-Chaouche, A. (2015). The 22 February 2014 Mw 4.1 Bordj-Menaïel Earthquake, Near Boumerdes-Zemmouri, North-Central Algeria. *Seismological Research Letters, 86*(3), 794–802.

Semmane, F., Benabdeloued, B., Heddar, A., & Khelif, M. (2017). The 2014 Mihoub earthquake (Mw4. 3), northern Algeria: Empirical Green's function analysis of the mainshock and the largest aftershock. *Journal of Seismology, 21*(6), 1385–1395.

Serpelloni, E., Vannucci, G., Pondrelli, S., Argnani, A., Casula, G., Anzidei, M., et al. (2007). Kinematics of the Western Africa-Eurasia plate boundary from focal mechanisms and GPS data. *Geophysical Journal International, 169*(3), 1180–1200.

Soumaya, A., Ayed, N. B., Rajabi, M., Meghraoui, M., Delvaux, D., Kadri, A., et al. (2018). Active faulting geometry and stress pattern near complex strike-slip systems along the Maghreb Region: Constraints on active convergence in the Western Mediterranean. *Tectonics, 37*(9), 3148–3173.

Toda, S., Stein, R. S., Richards-Dinger, K., & Bozkurt, S. B. (2005). Forecasting the evolution of seismicity in southern California: Animations built on earthquake stress transfer. *Journal of Geophysical Research: Solid Earth, 110*(B5). https://doi.org/10.1029/2004JB003415

Wildi, W. (1983). La chaîne tello-rifaine (Algérie, Maroc, Tunisie): Structure, stratigraphie et évolution du Trias au Miocène. *Revue De Géographie Physique Et De Géologie Dynamique, 24*(3), 201–297.

Yelles-Chaouche, A., Allili, T., Alili, A., Messemen, W., Beldjoudi, H., Semmane, F., et al. (2013). The new Algerian Digital Seismic Network (ADSN): Towards an earthquake early-warning system. *Advances in Geosciences, 36*, 31.

Yelles-Chaouche, A., Boudiaf, A., Djellit, H., & Bracene, R. (2006). La tectonique active de la région nord-algérienne. *Comptes Rendus Geoscience, 338*(1–2), 126–139.

Yelles-Chaouche, A., Djellit, H., Haned, S., Deramchi, A., Allili, T., Kherroubi, A., et al. (2007). The Algerian digital network. *European-Mediterranean Seismological Centre Newsletter, 22*, 7–8.

Yelles-Chaouche, A., Haned, A., Aidi, C., Beldjoudi, H., Kherroubi, A., Semmane, F., et al. (2017). The M w 5.0 Hammam Melouane earthquake (North Central Algeria) of 17 july 2013 in the context of the Tellian Atlas seismicity. *Pure and Applied Geophysics, 174*(4), 1601–1614.